5-6-2019

Ultrafast Processes in Phosphorene and Weyl semimetals

Fatemeh Nematollahi

ULTRAFAST PROCESSES IN PHOSPHORENE AND WEYL SEMIMETALS

by

FATEMEH NEMATOLLAHI

Under the Direction of Mark I. Stockman, PhD

ABSTRACT

In this dissertation, we study theoretically the nonlinear response of phosphorene and Weyl semimetals to an ultrafast laser pulse. We apply a femtosecond pulse and investigate the electron dynamics of the system in terms of the conduction band population. The optical pulse induces a finite conduction band (CB) population in the reciprocal space. In case of phosphorene, which is a semiconductor with a band gap ≈ 2 eV, the electron dynamics is highly irreversible which means that the residual electron CB population after the pulse is large and is comparable to the maximum conduction band population during the pulse. The large CB population appears near the Γ point where the dipole matrix elements between the valence band and the conduction band is strong. Also, the optical pulse causes both

interband and intraband electron dynamics during the pulse which a combination of both produces a net current through the system.

The electron dynamics of three-dimensional topological Weyl semimetals in an ultrafast linearly polarized pulse is coherent and highly anisotropic. For some directions of pulse polarization, the electron dynamics is irreversible, while for other directions of polarization, the electron dynamics is highly reversible. Such high anisotropy in electron dynamics is related to anisotropy in interband dipole matrix elements. The optical pulse also causes net charge transfer through the system. The transferred charge has highly anisotropic dependence on polarization direction with almost zero transferred charge for some directions.

Furthermore, we use the ultrafast pulse to illustrate the topological properties of Weyl semimetals such as chirality and topological resonance. The femtosecond pulse induces the topological resonance in Weyl semimetals. The topological resonance manifests itself in the distribution of the CB population. Such distribution in the conduction band is highly structured and is determined by the interference of the topological phase and the dynamic phase. The topological phase originates from the dipole. The topological resonance causes the Weyl points to be populated selectively, and this could be useful in applications such as optoelectronic devices.

INDEX WORDS: Ultrafast processes, 2D Material, Phosphorene, Weyl semimetal, TaAs, Ultrafast laser pulse, Topological resonance, Topological phase, Berry curvature, Electron dynamics, Current, Transferred charge, Electric field, Interband transition

ULTRAFAST PROCESSES IN PHOSPHORENE AND WEYL SEMIMETALS

by

FATEMEH NEMATOLLAHI

A Dissertation Submitted in Partial Fulfillment of the Requirements for the Degree of

Doctor of Philosophy

in the College of Arts and Sciences

Georgia State University

2019

ULTRAFAST PROCESSES IN PHOSPHORENE AND WEYL SEMIMETALS

by

FATEMEH NEMATOLLAHI

Committee Chair:	Mark I. Stockman
Committee:	Vadym Apalkov
	Mukesh Dhamala
	Sidong Lei

Electronic Version Approved:

Office of Graduate Studies

College of Arts and Sciences

Georgia State University

May 2019

DEDICATION

To my beloved parents,

and sisters,

and brothers.

ACKNOWLEDGMENTS

I would like to express my deepest gratitude to my supervisors Professor Mark Stockman and Professor Vadym Apalkov. This dissertation could not have been done without their guidance, support, and motivation. My sincerest gratitude and thanks also go to my committee members, Professor Vadym Apalkov, Professor Mukesh Dhamala, and Professor Sidong Lei for their effort in reading my dissertation and giving their fruitful comments. I would like to thank graduate advisor, Professor Murad Sarsour, the chair of physics and astronomy department, Professor Sebastien Lepine and all professors at Georgia state university for enriching classes.

I am extremely grateful to my parents, sisters, and brothers for their love, support, and encouragement. I am so lucky to have them in my life.

TABLE OF CONTENTS

LIST OF TABLES

LIST OF FIGURES

CHAPTER 1
INTRODUCTION

The availability of femtosecond laser sources has made great opportunities to explore the ultrafast and nonlinear response of matter to the external electric field. The laser pulse is considered ultrafast if the duration of pulse is shorter than all major relaxation times, which is typically between 1 to 1000 femtoseconds. Study the ultrafast process in materials, femtosecond and attosecond response to optical excitation, has been a subject of numerous theoretical and experimental research recently [3–10]. In relation to potential application of materials, it is very important to understand how these materials respond to applied external electric fields. Such strong fields, ~ 1 V/Å can strongly modify both optical and transport properties of materials within an optical cycle, resulting, for instance, in metallization of dielectric at a femtosecond time scale [11; 12]. Such metallization is observed as a finite charge transfer through a system during the pulse [6; 11]. The electron dynamics in such materials is highly reversible, i.e. that the residual conduction band (CB) population (the population of the conduction band at the end of the pulse) is small. Such reversibility is due to the large band gap, $\triangle \approx 10$ eV, of dielectric materials and $w \ll \frac{\triangle}{\hbar}$, where w is the frequency of the optical pulse.

In contrast, for materials with a small band gap, $w \gg \frac{\triangle}{\hbar}$, the electron dynamics in a strong external field is irreversible, which means that the residual CB population is large and is comparable with the maximum CB population during the pulse. For example, Ref.[4] reported the interaction of graphene with a strong ultrafast optical pulse with a duration of

a few femtoseconds. Graphene is a well known two-dimensional (2D) material which has attracted great attention both experimentally and theoretically due to unique optical and transport properties. The electron dynamics of graphene in a strong ultrafast field whose duration τ is less than the electron scattering time $\sim 10-100$ fs [10; 13; 14] is highly nonadiabatic and irreversible resulting in large CB population near the Dirac points at the end of the pulse. This irreversibility is related to the singularity of the interband coupling near the Dirac points. Also, it has been proposed [5] that attosecond strong-field interferometry in graphene, in the absence of magnetic field, reveals its chirality nature related to the Berry phase.

Zero band gap in graphene causes a relatively high off-current which limits its application in electronics devices such as transistor and logic circuits [15; 16]. As a result, significant effort has been devoted to identify alternative two-dimentional semiconductors. Similar to graphene, monolayer transition metal dichalcogenides (TMDCs) is a 2D material with hexagonal lattices. TMDCs have two sublattices consist of different atoms (metal and chalcogen) and have direct band gaps of $1.1-2.1$ eV [17; 18]. Ref. [19] theoretically introduces the valley polarization and the topological resonance in TMDCs induced by a circularly-polarized ultrafast pulse. The presence of valley polarization can be used in data processing in PHz-band optoelectronics, and the concept of topological resonance stimulates developments in topological strong-field optics of solids.

Another two-dimensional semiconductor which has attracted considerable attention is a monolayer of phosphorene. Since phosphorene has a relatively large band gap, it could

have a potential application in electronic devices. In this dissertation, we theoretically study the dynamics of electrons in 2D-phosphorene under the interaction of the ultrafast and strong optical pulses. Also, we studied the ultrafast phenomenon in three-dimensional topological Weyl semimetals, which can be considered as a three dimensions of graphene, to underestand how we can modify the electronic properties of graphene in three dimensions.

The dissertation starts with an introduction to the model and equations and then it follows by introducing the properties of phosphorene and proceeds the study of ultrafast process in phosphorene. We report the non-linear response of phosphorene to an ultrafast optical pulse with a duration of a few femtoseconds. The results of this study could pave the way for experimental studies on optical responses of phosphorene nanodevices. In the following chapters, we theoretically study the electron dynamics of three dimensional topological Weyl semimetals in the ultrafast laser field. In chapter four, we employ the effective Hamiltonian model of Weyl semimetals to describe the behavior of electron near the Weyl points in an external electric field. We apply both linearly and circularly polarized optical pulse. The fifth chapter is related to the topological properties of Weyl semimetals. We study the topological resonance in Weyl semimetals. We apply both linearly and circularly polarized pulse to induce the conduction band CB population in reciprocal space. We use the topological phase to describe the texture of the CB population in the momentum space. Finally, using a circularly polarized optical pulse, we propose self-referenced interferometry in reciprocal space which reveals the intrinsic chirality of Weyl points in Weyl semimetals.

CHAPTER 2
METHODS AND EQUATIONS

2.1 Theory of solids in strong ultrashort laser fields

In this dissertation we study the interaction of ultrashort, ultrastrong laser pulses with solids. Ultrashort laser pulses are considered to be those whose pulse duration is less than a few picoseconds (10^{-12}s) long. The electric field in an ultrastrong laser pulse is of the order of volts per angstrom which is comparable to the internal electric fields in solids. The propagation of the incident pulse in this case is characterized by the angle of incident, θ. We usually determine the electron dynamics and pulse propagation, and their numerical solution for the normally incident pulse, ($\theta = 0$). The laser pulse is characterized by the following parameters: the duration of the pulse τ and the amplitude of the pulse F_0. In this dissertation we consider only coherent electron pulse, $\tau \lesssim 10$ (fs).

The electron dynamics in the external optical field is described by the time-dependent Schrödinger equation (TDSE)

$$i\hbar\frac{d\psi}{dt} = \mathcal{H}\psi, \tag{2.1}$$

where

$$\mathcal{H} = \mathcal{H}_0 + e\mathbf{F}(t)\mathbf{r}. \tag{2.2}$$

Here, $\mathcal{H}_0$ is field free electron Hamiltonian, $\mathbf{F}$ is field, e is electron charge and $\mathbf{r}$ is a vector position. The applied optical pulse generates both interband and intraband electron dynamics. The interband electron dynamics causes redistribution of electrons between the valence and

conduction bands, while the intraband electron dynamics determines the electron dynamics within a single band. Such intraband dynamics provides the main contribution to the charge transfer, which is studied in the following chapters. The intraband electron dynamics is described by the universal acceleration theorem [20] of the form

$$\hbar \frac{d\mathbf{k}}{dt} = e\mathbf{F}(t), \tag{2.3}$$

which has the following solution

$$\mathbf{k}_T(\mathbf{q}, t) = \mathbf{q} + \frac{e}{\hbar} \int_{-\infty}^{t} \mathbf{F}(t_1) dt_1, \tag{2.4}$$

where $\mathbf{q}$ is the initial wave vector. Such intraband dynamics in the reciprocal space is incorporated into the corresponding wave functions through the Houston functions [21] of the form

$$\Phi_{\alpha q}^{(H)}(\mathbf{r}, t) = \psi_\alpha(\mathbf{k}_T(\mathbf{q}, t)) e^{-\frac{i}{\hbar} \int_{-\infty}^{t} dt_1 E_\alpha \left(\mathbf{k}_T(q, t_1) \right)}. \tag{2.5}$$

The Houston functions completely describe the intraband electron dynamics and are used below as a basis, so that the general solution of the time dependent Schrödinger equation (2.1) can be described as follows

$$\psi_q(\mathbf{r}, t) = \sum_{\alpha = v,c} \beta_{\alpha q}(t) \Phi_{\alpha q}^{(H)}(\mathbf{r}, t), \tag{2.6}$$

where v and c denote the valence band and the conduction bands, respectively.

The expansion coefficients $\beta_{\alpha q}(t)$ satisfy the following system of differential equations

$$\frac{d\beta_{\alpha q}}{dt} = -\frac{i}{\hbar} \mathbf{F} \sum_{\alpha_1 \neq \alpha} Q_{\alpha \alpha_1}(t) \beta_{\alpha_1 q}(t), \tag{2.7}$$

where $\alpha, \alpha_1 = 1, 2, 3, ..., n$. The time-dependent matrix $Q_{\alpha\alpha_1}(t)$ is determined by the component of the dipole matrix elements $D_{\alpha\alpha_1}(\mathbf{k})$ between bands α and α_1

$$Q_{\alpha\alpha_1}(t) = D_{\alpha\alpha_1}[\mathbf{k}_T(\mathbf{q}, t)] \times e^{-\frac{i}{\hbar}\int_{-\infty}^{t} dt_1 \Big(E_\alpha(\mathbf{k}_T(\mathbf{q}, t_1)) - E_{\alpha_1}(\mathbf{k}_T(\mathbf{q}, t_1)) \Big)}, \tag{2.8}$$

where

$$D_{\alpha\alpha_1}(\mathbf{k}) = \langle \psi^{(\alpha)}_{\mathbf{k}} | e\mathbf{r} | \psi^{(\alpha_1)}_{\mathbf{k}} \rangle = \frac{\hbar}{i} \frac{\langle \Phi^{(\alpha_1)} | \hat{V} | \Phi^{(\alpha)} \rangle}{[E_{\alpha_1}(\mathbf{k}) - E_\alpha(\mathbf{k})]}. \tag{2.9}$$

Here $\hat{V}$ is the matrix element of the velocity operator

$$\hat{\mathbf{V}} = \frac{1}{\hbar} \frac{\partial \mathcal{H}_0}{\partial \mathbf{K}}. \tag{2.10}$$

The system of equations (2.7) describes the interband electron dynamics. We characterize the interband dynamics, i.e., the solution of the system of equations (2.7), by the time-dependent conduction band populations $|\beta_{c,q}(t)|^2$. We also define the time-dependent total population of the conduction bands

$$\mathcal{N}_{CB,\alpha}(t) = \sum_{q,j} |\beta^{(j)}_{\alpha,q}(t)|^2, \tag{2.11}$$

where α refers to the conduction bands. The index j corresponds to the initial conditions.

The interband and intraband electron dynamics results not only in redistribution of electrons between the valence and conduction bands but also in generation of an electric

current, which can be calculated from the following expression

$$J_j(t) = e \int d\mathbf{q} \sum_{\alpha_1=v,c} \sum_{\alpha_2=v,c} \beta^*_{\alpha_1 q}(t) V_j^{\alpha_1\alpha_2} \beta_{\alpha_2 q}(t), \tag{2.12}$$

where $j = x, y, z$ and $V_j^{\alpha_1\alpha_2}$ are the matrix elements of the velocity operator (2.10).

The generated current results in the charge transfer through the system, which is determined by

$$Q_{tr} = \int_{-\infty}^{\infty} dt J(t). \tag{2.13}$$

CHAPTER 3
PHOSPHORENE IN ULTRAFAST LASER FIELD

3.1 Introduction

Two-dimensional (2D) materials such as graphene, MoS_2 and silicene, are a focus of theoretical and experimental research because of their potential applications into next-generation electronic devices [22–25]. Graphene has the honeycomb crystal structure with unique relativistic energy dispersion and chiral electron states and is still the most prominent two-dimensional crystal. However, the lack of bandgap in graphene, has motivated an intensive of works on semiconducting 2D materials [26–29] which can have application in electronic devices and photodetectors. For other 2D materials, such as silicene or germanene, which have crystal structure similar to graphene, a finite but small bandgap is opened due to relatively large spin-orbit interaction. Such band gap can be controlled by an external electric field. The discovery of monolayer group-VI transition metal dichalcogenides (TMDs), (M=Mo, W; X=S, Se) [30; 31] which have been shown to possess direct energy gaps in the near-infrared to the visible spectral region, has opened up a new window for photonics and optoelectronics.

In this relation, phosphorene has attracted intense attention recently. Phosphorene, an atomic layer of black phosphorous, was realized by the mechanical exfoliation from the layered crystal of black phosphorous (BP) in 2014. It is a single component two-dimensional (2D) crystal following graphene and silicene. Phosphorene has an orthorhombic crystal structure, where the phosphorous atom is directly bonded to three other neighboring atoms via covalent bonds thus forming a puckered honeycomb structure because of hybridization, as

shown in Figure 3.1 [2]. Single-layer black phosphorene is a direct-gap semiconductor with a predicted band gap of 2 eV [32]. The band gap decreases with an increasing number of layers and is 0.3 eV for the bulk phase. Unlike the indirect-to-direct band gap transition in TMDCs, the band topology remains the same with changing thickness and all few-layer phosphorene samples are direct semiconductors with the conduction band minimum at the Γ point. The thickness independent band topology of phosphorene is important for its potential photonics and optoelectronics applications. The gap value $(0.3 - 2)$ eV is typically smaller than those of the TMDC compounds $(1.1 - 2.5)$ eV but larger than the semimetallic graphene, enabling phosphorene to possess a moderate on/off current ratio $(10^4 - 10^5)$ [33; 34] while having a sufficiently large carrier mobility (around 1000 (cm^2/V.s)) [33] suitable for many applications. Based on semiconducting nature, researchers have fabricated few-layer phosphorene field-effect transistors (FET) with on/off current ratios as high as 10^4 and carrier mobility levels as high as 1000 (cm^2/V.s) at room temperature [34; 35]. In this chapter we theoretically study the electron dynamics of phosphorene in an ultrafast optical pulse. The results reveal the potential application of monolayer phosphorene in ultrafast optoelectronics and electronics devices.

3.2 Phosphorene four-band tight-binding model

The tight-binding (TB) Hamiltonian proposed for phosphorene is given by [2]

$$H_k = \begin{pmatrix} 0 & A_k & B_k & C_k \\ A_k^* & 0 & D_k & B_k \\ B_k^* & D_k^* & 0 & A_k \\ C_k^* & B_k^* & A_k^* & 0 \end{pmatrix}, \tag{3.1}$$

where

$$A_k = t_2 + t_5 e^{-ik_a}, \tag{3.2}$$

$$B_k = 4t_4 e^{-i(k_a - k_b)/2} \cos(k_a/2) \cos(k_b/2), \tag{3.3}$$

$$C_k = 2e^{ik_b/2} \cos(k_b/2)(t_1 e^{-ik_a} + t_3), \tag{3.4}$$

$$D_k = 2e^{ik_b/2} \cos(k_b/2)(t_1 + t_3 e^{-ik_a}). \tag{3.5}$$

In each zigzag chain, the connection in the lower or upper layers are represented by t_1 hopping integrals, and the connection between a pair of upper and lower zigzag chains are illustrated by t_2 hopping integrals. Further, t_3 corresponds to the hopping integrals between the nearest sites of a pair of zigzag chains in the upper or lower layer, and t_4 represents the hopping integrals between the next nearest neighbor sites of a pair of upper and lower zigzag chains. Finally, t_5 is the hopping integrals between two atoms on the upper and lower zigzag chains that are farthest from each other. The specific values of these hopping integrals as suggested in [36] are: $t_1 = -1.220$ eV, $t_2 = 3.665$ eV, $t_3 = -0.205$ eV, $t_4 = -0.105$ eV and

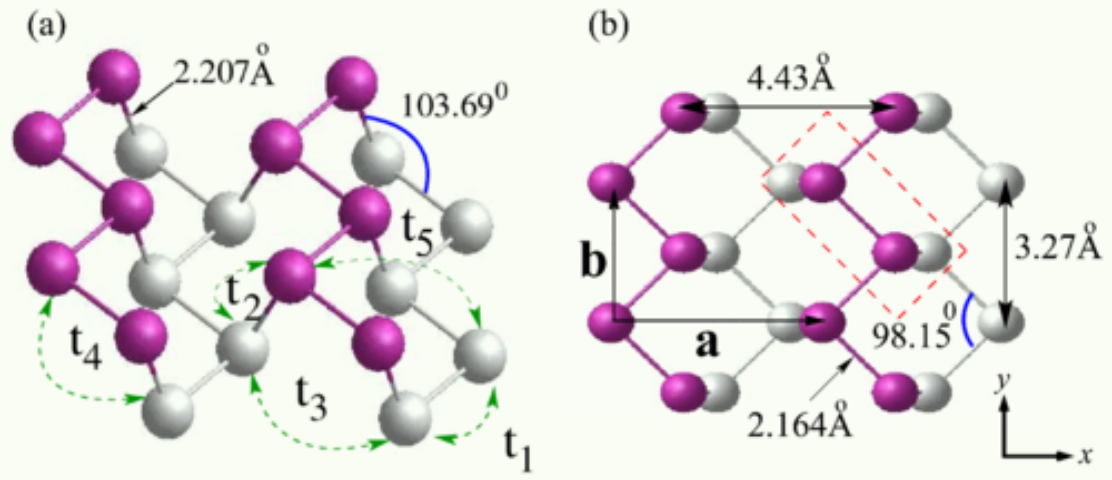

Figure 3.1 (Color online) (a) Crystal structure and hopping integrals t_i of phosphorene for the TB model. (b) Top view . Note that the gray balls indicate the phosphorus atoms in the upper (lower) layer. The primitive unit cell containing four atoms is shown by dotted rectangle. The parameters for the bond angles and unit cell lengths are taken from Ref.[1]. This figure is taken from Ref. [2]

$t_5 = -0.055$ eV.

As shown in Figure 3.1(b) the unit cell of the monolayer phosphorene is a rectangle containing four phosphorous atoms.

Here $k_a = \mathbf{k}.\mathbf{a}$ and $k_b = \mathbf{k}.\mathbf{b}$, where $\mathbf{a} = a\mathbf{x}$ and $\mathbf{b} = b\mathbf{y}$ are the primitive translation vectors of the structure displayed in Figure 3.2(a).

From the tight-binding Hamiltonian (3.1) we can find the energy spectrum, $E_\alpha(k)$, and the corresponding wave functions, $\psi_\alpha(k)$. Here $\alpha = 1, 2, 3, 4$ where $\alpha = 1, 2$ correspond to two valence bands and $\alpha = 3, 4$ correspond to two conduction bands. The band gap of phosphorene is ≈ 2 eV.

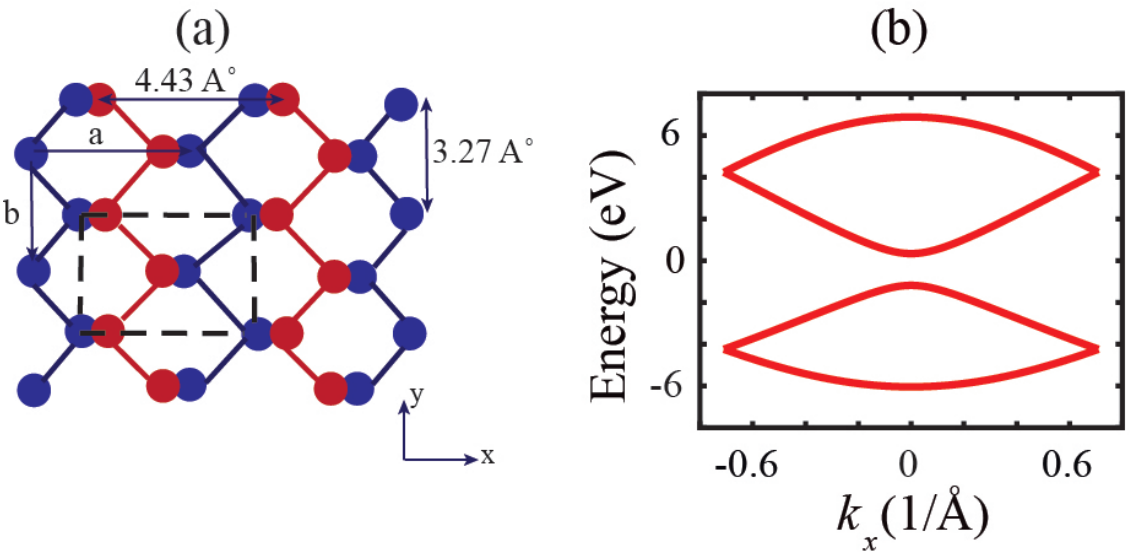

Figure 3.2 (Color online) (a) Lattice structure of 2D phosphorene. The red and blue dots represent phosphorous atoms in the upper and lower layers, respectively. The dashed lines show the primitive unit cell, which contains four atoms. The primitive vectors a and b are also shown. The parameters for the unit cell lengths are taken from Ref [1]. (b) Electronic band structure of phosphorene.

3.3 Phosphorene in an external strong electric field

We assume that an ultrashort optical pulse propagates along k_z, where k_z is the out of plane quasimomentum and incident normally on a phosphorene , and has the following profile:

$$F(t) = F_0 e^{-u^2}(1 - 2u^2), \tag{3.6}$$

where F_0 is the amplitude of the pulse, $u = t/\tau$, and τ is the pulse's duration. The experimentally realized profile of the ultrastrong optical pulse can be found in Ref.[12].

For the shape of the pulse given by Eq.(3.6), the area under the pulse is always zero, $\int_{-\infty}^{t} F(t)dt = 0$. Below we assume that $\tau = 1$ fs, which corresponds to the carrier frequency of $w \approx 1.5$ eV/$\hbar$. For such ultrashort pulse, the duration of which is less than the

characteristic electron scattering time $\sim 10 - 100$ fs, the electron dynamics during the pulse is coherent and can be described by the time-dependent Schrödinger equation.

The system of equations (2.7) describes the interband electron dynamics. We solve this system numerically under the following initial conditions: $(\beta_1, \beta_2, \beta_3, \beta_4) = (1, 0, 0, 0)$ and $(\beta_1, \beta_2, \beta_3, \beta_4) = (0, 1, 0, 0)$, which correspond to initially occupied valence bands, i.e., bands 1 and 2. We characterize the interband dynamics, i.e., the solution of the system of equations (2.7), by the time-dependent conduction band populations $|\beta_{3,q}|^2$ and $|\beta_{4,q}|^2$.

3.4 Results and Discussion

The interband electron dynamics is characterized by electron redistribution between the valence and conduction bands and finally by finite conduction bands' populations. Such CBs populations are mainly determined by the strength of the interband dipole couplings, while the distribution of the CB population in the reciprocal space depends on the profile of the interband dipole matrix element in the reciprocal space. For example, in graphene, the interband dipole coupling is highly nonuniform in the reciprocal space and is singular at the Dirac points. Such singularities result in highly nonuniform electron distribution in the reciprocal space with hot spots near the Dirac points. In phosphorene, which has a finite bandgap, ≈ 2 eV, the interband dipole matrix elements do not have any singularity in the reciprocal space. The interband dipole coupling is the strongest between the highest valence band and the lowest conduction band, i.e., between the bands 2 and 3. The corresponding dipole matrix element, D_{23}, is shown in Figure 3.3 (b) as a function of the reciprocal vector.

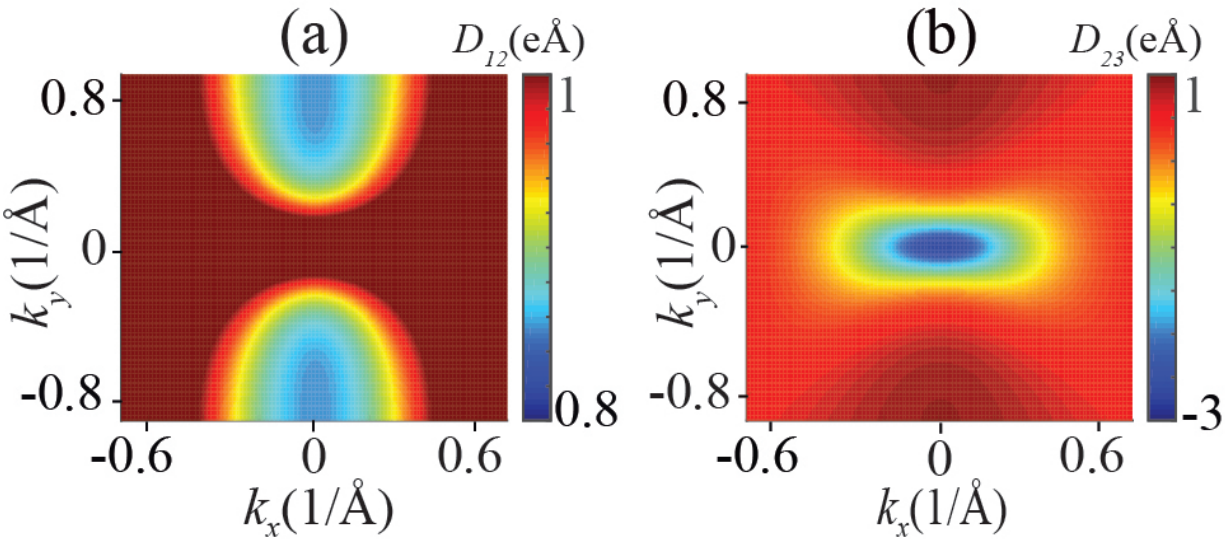

Figure 3.3 (Color online) Interband dipole matrix elements D_{12} and D_{23}. The dipole matrix elements are shown as functions of the wave vector $\mathbf{k}$. Here D_{12} is the dipole matrix element between two valence bands, 1 and 2, while D_{23} is the dipole matrix element between the highest energy valence band (band 2) and the lowest energy conduction band (band 3). The dipole matrix element $|D_{23}|$ has a maximum at the Γ point.

The dipole matrix element D_{23} has a well pronounced maximum at the Γ point, $(0, 0)$. The other dipole matrix elements are almost constant within the whole Brillouin zone, see, for example, the dipole matrix element D_{12} shown in Figure 3.3 (a). The maximum of the dipole matrix element D_{23} between the lowest CB and the highest VB results in specific distribution of the CB population in the reciprocal space. This is due to the fact that the strongest interband mixing occurs only when an electron, which is drifting through the reciprocal space according to the acceleration theorem, is near the Γ point, $(0, 0)$.

The interband electron dynamics can be characterized in terms of the time evolution of the total CB populations. The total CB populations of the first and the second CBs are shown in Figure 3.4 for different amplitudes of the pulse. The data illustrates that the

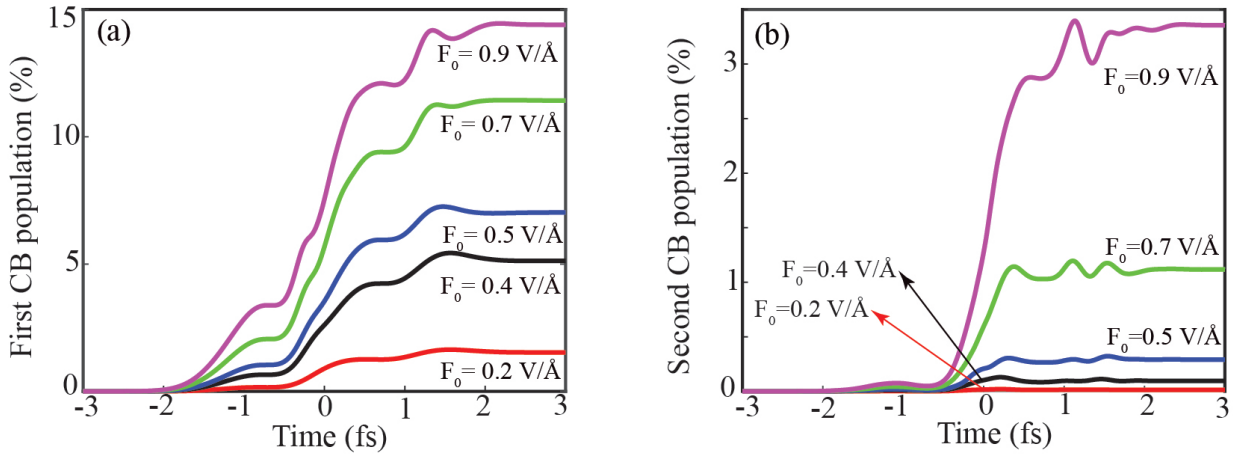

Figure 3.4 (Color online) Conduction band population as a function of time. (a) Population of the first conduction band. (b) Population of the second conduction band. The peak fields are indicated on the graph.

electron dynamics is highly irreversible, i.e., the maximum CB population during the pulse is comparable to the residual CB population after the pulse. This dynamics is similar to the one in gapless graphene. Although the phosphorene monolayer has a finite bandgap, $\Delta \approx 2$ eV, the gap is closed at the field amplitude $\approx \Delta/a \approx 0.4$ V/Å, where $a = 4.43$ Å.

The electron dynamics is highly irreversible, i.e., the system does not return to its initial state, which has zero CB populations, see Figure 3.4. For $F_0 \lesssim 0.7$ V/Å, the total population of the second CB is an order of magnitude smaller than the total population of the first CB, for example, at $F_0 = 0.7$ V/Å, the residual CB population of the first band is 12 times lager than the residual CB population of the second band. At higher field amplitudes, the difference between the CB populations of the two bands becomes less pronounced. For example, at $F_0 = 0.9$ V/Å, the residual CB population of the first CB becomes only four times larger than the residual CB population of the second CB.

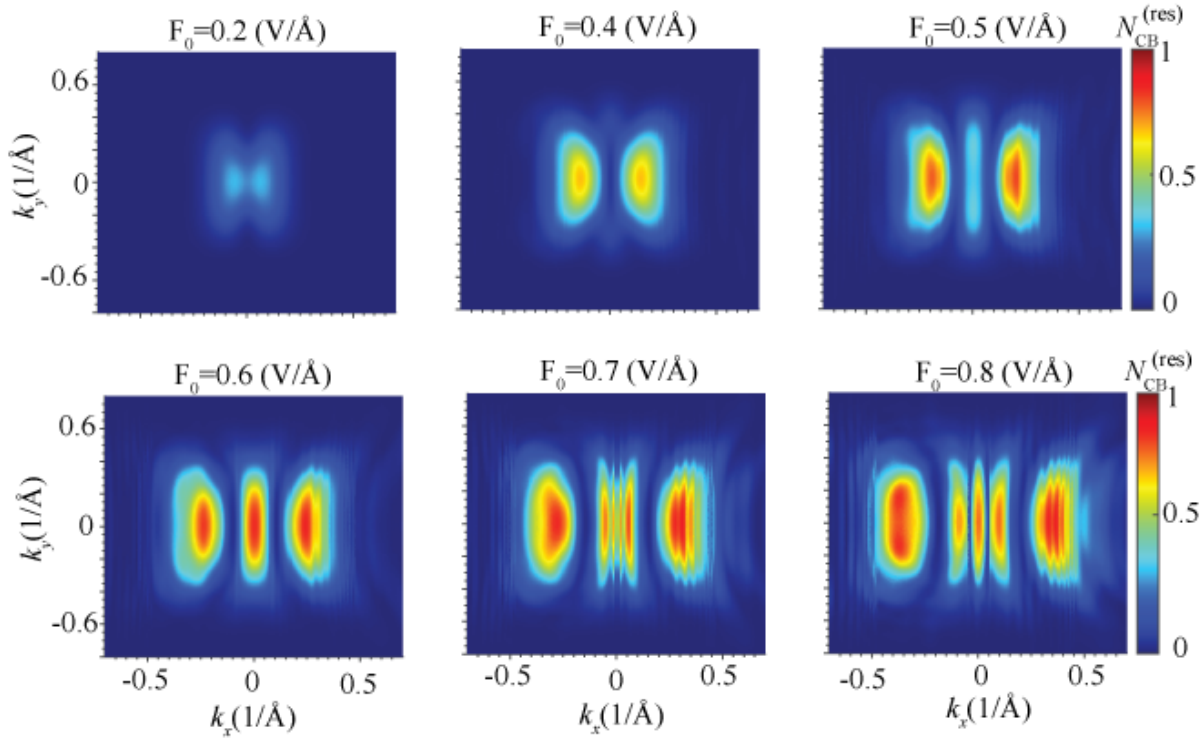

Figure 3.5 (Color online) Residual population of the first conduction band as a function of wave vector **k** for different amplitudes F_0 of the optical pulse, as indicated. The pulse is polarized along axis x.

In Figure 3.5, the residual CB population, i.e., the electron CB population after the pulse, is shown for different amplitudes of the optical pulse. The data show that large CB population is localized near the Γ point. The hot spots near the Γ point are located symmetrically with respect to k_y-axis. The origin of such hot spots is the same as in graphene. They are due to interference, which happens when an electron passes twice through the Γ point during the

pulse. The structure shown in Figure 3.5 is similar to the one that was observed in graphene [4], but with one fundamental difference. In phosphorene, if an electron goes directly through the Γ point then the corresponding points of the hot spots have a maximum. In graphene, if an electron goes directly through the Dirac point then the corresponding intensity at the hot spots is zero. This is because the dipole matrix element has a singularity in graphene but just a maximum in phosphorene. The CB population of the first CB is shown in Figure 3.5. The CB population of the second band is a few times smaller than the CB population of the first band. Its distribution in the reciprocal space also shows the hot spots but they are much less pronounced.

The time evolution of the CB population in the reciprocal space is shown in Figure 3.6. The emergence of the hot spots as an electron passes through the region with large interband coupling is clearly visible. This behavior supports the above statement that the hot spots in the CB population distribution are due to electron passages through the region with large interband dipole matrix elements. The hot spots are localized due to interference, which happens after two passages through the region with large interband coupling.

The number of hot spots in the CB population distribution increases with increasing field amplitude. This is because for a larger field amplitude, an electron travels a longer distance in the reciprocal space, see Eq. (2.4).

The total residual CB populations for the first and second CBs, $N_1^{(res)}$ and $N_2^{(res)}$, respectively, are shown in Figure 3.7 as the functions of the field amplitude. The residual CB population of the first band monotonically increases with field. Even at small field am-

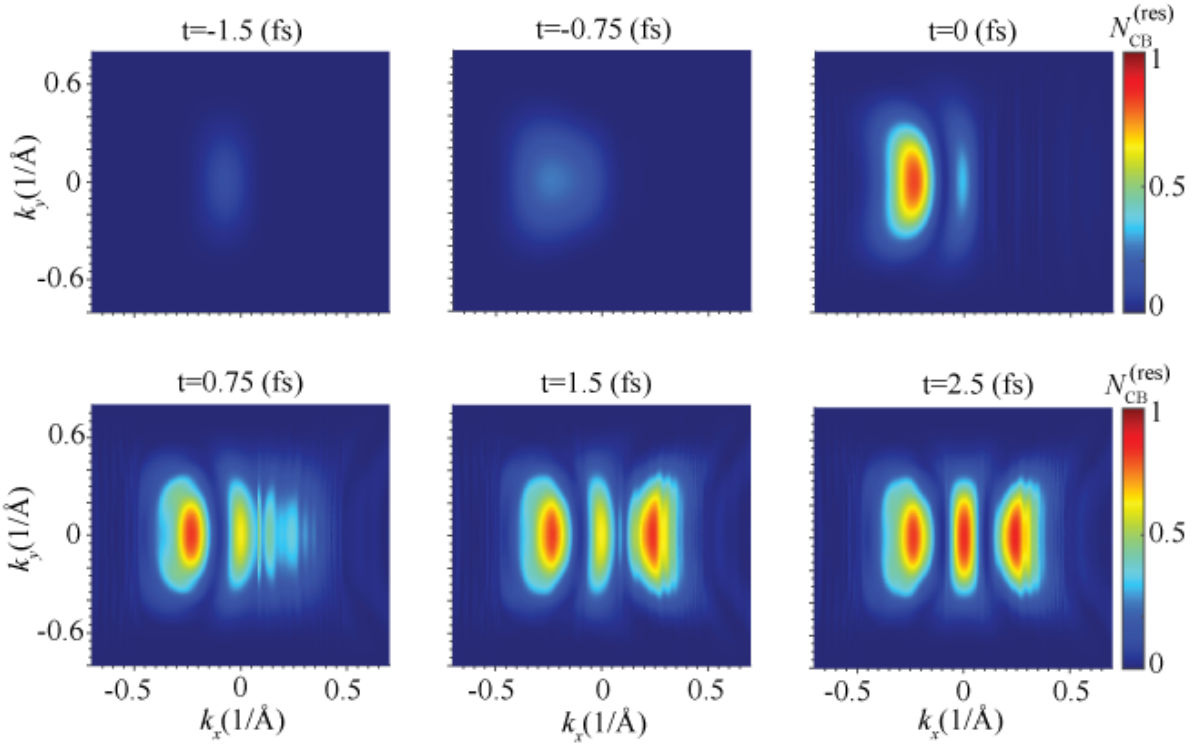

Figure 3.6 (Color online) Population of the first conduction band as a function of wave vector at different moments of time. The amplitude of the optical pulse is $F_0 = 0.6$ V/Å. Different colors correspond to different values of the conduction band population as shown in the figure.

plitudes, the residual CB population is relatively large. The residual CB population of the second band, $N_2^{(res)}$, is almost zero at $F_0 < 0.4$ V/Å and then it strongly increases with pulse intensity. This behavior is also illustrated in Figure 3.7(b), where the ratio $N_1^{(res)}/N_2^{(res)}$ is shown. Here the transition from a large ratio, ~ 80, to a small ratio, ~ 5, occurs with increasing pulse amplitude. Both interband and intraband electron dynamics generate an

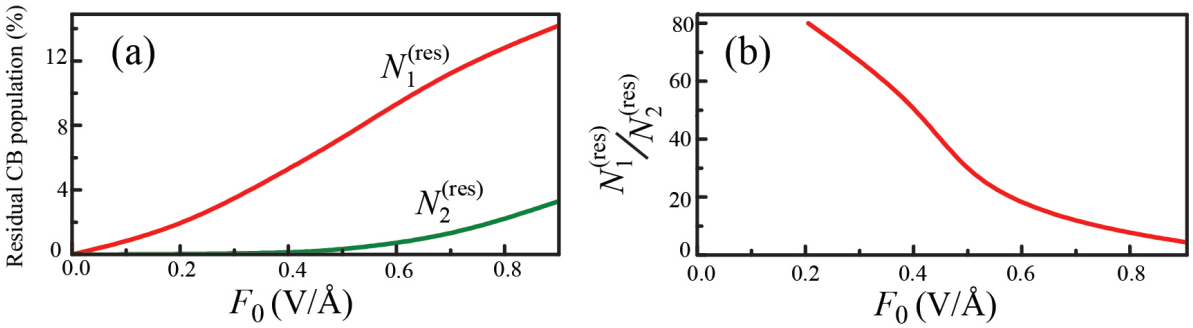

Figure 3.7 (Color online) (a) Residual conduction band population for the first, $N_1^{(res)}$, and the second, $N_1^{(res)}$, conduction bands as a function of the peak electric field, F_0. (b) Ratio of the residual conduction band populations, $N_1^{(res)}/N_2^{(res)}$.

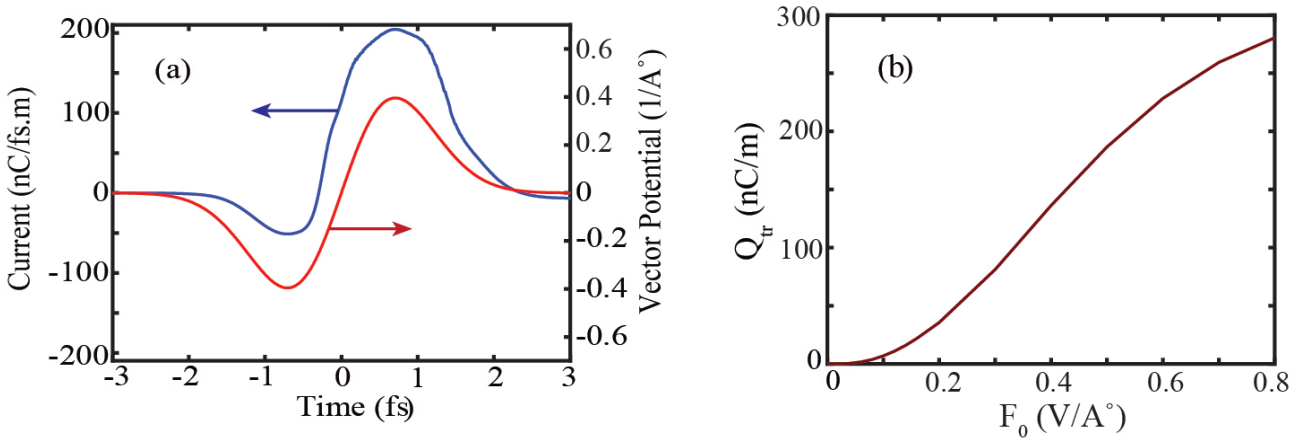

Figure 3.8 (Color online) (a) Electric current density and vector potential, $\int F(t)dt$, as a function of time. (b) Transferred charge density through phosphorene monolayer as a function of F_0.

electric current through the system. Such current can be found from Eq. (2.12). The electric current has two contributions: interband current and intraband current. Usually, and also in our case of phosphorene, the main contribution to the electric current comes from the intraband term. The time dynamics of the electric current is shown in Figure 3.8(a). The current follows the time integral of the electric field, i.e., the vector potential, $\int F(t)dt$. This

behavior supports the above statement that the main contribution to the net electric current comes from the intraband term. The residual electric current is zero, which corresponds to residual electron population distribution that is symmetric with respect to k_y axis. The area under the current versus time graph is the charge transferred through the system during the pulse, see Eq. (2.13). The transferred charge as a function of field amplitude is shown in Figure 3.8 (b). The transferred charge is positive for all field amplitudes. The positive sign of Q_{tr} means that the direction of the charge transfer is the same as the direction of the field maximum. This behavior is different from graphene, for which the transferred charge changes its sign from positive to negative with increasing pulse's intensity.

At small field amplitudes the transferred charge behaves as

$$Q_{tr} \propto F_0^3. \tag{3.7}$$

3.5 Conclusion

The electron dynamics in a single layer of black phosphorus, i.e., phosphorene, in a strong field of an ultrashort optical pulse is highly irreversible, which means that the residual CB population is comparable to the maximum CB population during the pulse. Although the phosphorene has a relatively large bandgap, ≈ 2 eV, the irreversible electron dynamics in phosphorene is similar to the electron dynamics in other 2D materials, such as gappless graphene, silicene or germanene. The residual CB population in phosphorene is relatively large. It is about 20 % at the field amplitude $F_0 = 0.9$ V/Å. Here the population of the first CB is about 15 % while the population of the second CB band is 4 %. The distribution

of the CB population in the reciprocal space shows hot spots that are located near the Γ point. These hot spots are due to two factors. The first one is that the interband dipole coupling has a maximum at the Γ point. Thus, during an electron field-induced transport in the reciprocal space the strongest interband coupling occurs when the electron passes the vicinity of the Γ point. The second factor, which determines the formation of the hot spots, is that the electron passes twice the Γ point. Such double passage results in formation of specific interference patterns in the CB population distribution. This behavior shows that, for a general system, by looking at the CB population distribution in the reciprocal space we can identify the positions of the maxima of the interband couplings in the system.

The electron dynamics in phosphorene is also characterized by the charge transfer through the system, which is proportional to the residual polarization of the phosphorene monolayer. The charge transfer through phosphorene occurs in the direction of the field maximum for all field amplitudes.

CHAPTER 4

NON-LINEAR RESPONSE OF WEYL SEMIMETLAS TO ULTRAFAST LASER FIELD

4.1 Introduction

In this chapter we theoretically study the electron dynamics of Weyl semimetals in ultrafast laser pulse. Weyl semimetals are gapless materials whose quasiparticle excitations are Weyl fermions with definite chirality [37]. Such materials are characterized by linear band crossing points called Weyl points near the Fermi energy. Due to the no-go theorem [38; 39], Weyl points appear as a pair with opposite chirality separated in the Brillouin zone and they are connected through the Fermi arcs. Figure 4.1 shows schematically the Weyl semimetal state which is including the Weyl points and Fermi arcs. Weyl points behave as a source or sink of Berry curvature of Bloch wave functions in momentum space. Weyl points with opposite chirality are mirror symmetric, while those related by rotation and time reversal symmetries posse the same chirality. Unique characteristics of Weyl semimetals such as energy dispersion and chirality of Weyl fermions causes interesting optical phenomena. To name, but a few, vally polarization which is induced by light in nonlinear Weyl semimetals [40], photocurrent in Weyl semimetals [41] and photoinduced anomalous Hall effects [42].

Here we study the nonlinear response of Weyl semimetals to ultrafast optical pulse. This study can be used to understand the behavior of electron in high-field devices and generally can be used to guide optoelectronic applications. We theoretically study the ultrafast dynamics of Weyl semimetals in a linearly and circularly-polarized pulse with a duration of a

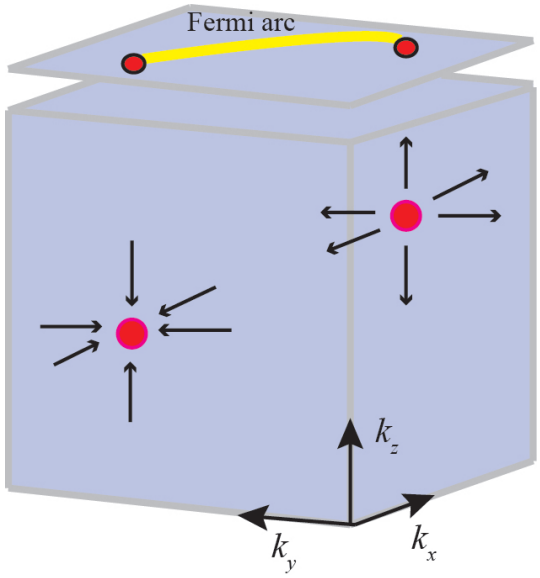

Figure 4.1 (Color online) A schematic of the Weyl semimetal state. Weyl points with opposite chirality separated in momentum space and they are just connected through the Fermi arcs.

few femtoseconds. This study make it possible to investigate basic questions concerning the out-of equilibrium behavior of Weyl fermions.

4.2 Model and main equations

We assume that the ultrafast optical pulse with a duration of a few femtoseconds propagates normally on the Weyl semimetal. For the field-free Hamiltonian we use the lower-energy approximation of the full Hamiltonian of the system in the reciprocal space near the Weyl points. The corresponding Hamiltonian has the following form [43]

$$\mathcal{H}_0 = E_0\mathbb{I} + \mathbf{v}_0.\mathbf{q}.\mathbb{I} + v_x q_x \sigma_x + v_y q_y \sigma_y + v_z q_z \sigma_z, \tag{4.1}$$

where $\mathbb{I}$ is the identity matrix, $\mathbf{q} = \mathbf{k} - \mathbf{k}_0$, $\mathbf{k}_0$ is the position of the Weyl point in the reciprocal space, $\mathbf{k}$ is the electron wave vector , and σ_i are three Pauli matrices. Here $\mathbf{v}_0 =$

$(v_{0,x}, v_{0,y}, v_{0,z})$, v_x, v_y, v_z, and E_0 are the parameters of the Hamiltonian. The corresponding conduction and valence band energy dispersions are the following

$$E_c = \hbar(v_{0x}q_x + v_{0y}q_y + v_{0z}q_z + \sqrt{\mu}), \tag{4.2}$$

for the conduction band and

$$E_v = \hbar(v_{0x}q_x + v_{0y}q_y + v_{0z}q_z - \sqrt{\mu}), \tag{4.3}$$

for the valence band. Here $\mu = v_x^2q_x^2 + v_y^2q_y^2 + v_z^2q_z^2$.

Substituting the wave functions found from the field-free Hamiltonian (4.1) into Eq. (2.9), we obtain the following expressions for the dipole matrix elements

$$\begin{aligned} D_x(\mathbf{k}) &= \frac{e}{2i\mu}\frac{-v_x}{\sqrt{v_x^2q_x^2 + v_y^2q_y^2}}\left(v_xq_xv_zq_z + iv_yq_y\sqrt{\mu}\right), & (4.4)\\ D_y(\mathbf{k}) &= \frac{e}{2i\mu}\frac{-v_y}{\sqrt{v_x^2q_x^2 + v_y^2q_y^2}}\left(v_yq_yv_zq_z - iv_xq_x\sqrt{\mu}\right), & (4.5)\\ D_z(\mathbf{k}) &= \frac{ev_z}{2i\mu}\sqrt{v_x^2q_x^2 + v_y^2q_y^2}. & (4.6) \end{aligned}$$

The system of equations (2.7) is solved numerically with the following initial conditions $(\beta_{vq}, \beta_{cq}) = (1, 0)$. This condition means that in the initial state, the valence band is occupied and the conduction band is empty.

The matrix elements of the velocity operator, see Eq. (2.10), calculated between the valence

and conduction band states are given by the following expressions

$$V_x^{vv} = \frac{1}{\hbar}\left[v_{0x} - \frac{v_x^2 q_x}{\sqrt{\mu}}\right], \tag{4.7}$$

$$V_x^{cc} = \frac{1}{\hbar}\left[v_{0x} + \frac{v_x^2 q_x}{\sqrt{\mu}}\right], \tag{4.8}$$

$$V_x^{vc} = V_x^{*cv} = \frac{1}{\hbar}\frac{1}{\sqrt{\mu - v_z^2 q_z^2}}\frac{v_x}{\sqrt{\mu}} \times \left[- v_x v_z q_x q_z + i\sqrt{\mu} v_y q_y\right], \tag{4.9}$$

$$V_y^{vv} = \frac{1}{\hbar}\left[v_{0y} - \frac{v_y^2 q_y}{\sqrt{\mu}}\right], \tag{4.10}$$

$$V_y^{cc} = \frac{1}{\hbar}\left[v_{0y} + \frac{v_y^2 q_y}{\sqrt{\mu}}\right], \tag{4.11}$$

$$V_y^{vc} = V_y^{*cv} = \frac{1}{\hbar}\frac{1}{\sqrt{\mu - v_z^2 q_z^2}}\frac{v_y}{\sqrt{\mu}} \times \left[- v_y v_z q_y q_z - i\sqrt{\mu} v_y q_y\right], \tag{4.12}$$

$$V_z^{vv} = \frac{1}{\hbar}\left[v_{0z} - \frac{v_z^2 q_z}{\sqrt{\mu}}\right], \tag{4.13}$$

$$V_z^{cc} = \frac{1}{\hbar}\left[v_{0z} + \frac{v_z^2 q_z}{\sqrt{\mu}}\right], \tag{4.14}$$

$$V_z^{vc} = V_z^{cv} = \frac{v_z}{\hbar}\left[\sqrt{\mu - v_z^2 q_z^2}\right]. \tag{4.15}$$

4.3 Results and discussions

We present the results for TaAs, which is a body-centered tetragonal lattice system, see Figure 4.2(a), with lattice constants $a = b = 3.437$ Å along x and y direction, respectively and $c = 11.646$ Å along z direction. TaAs has two sets of Weyl points with following coordinates: $(\pm 0.0072, 0.4827, 1.0000)$ for the first pair, W_1 and $(\pm 0.0185, 0.2831, 0.6000)$ for the second pair, W_2. Here the coordinates of the points are given in units of reciprocal lattice vectors. The energy dispersion of TaAs near the second Weyl point is illustrated in

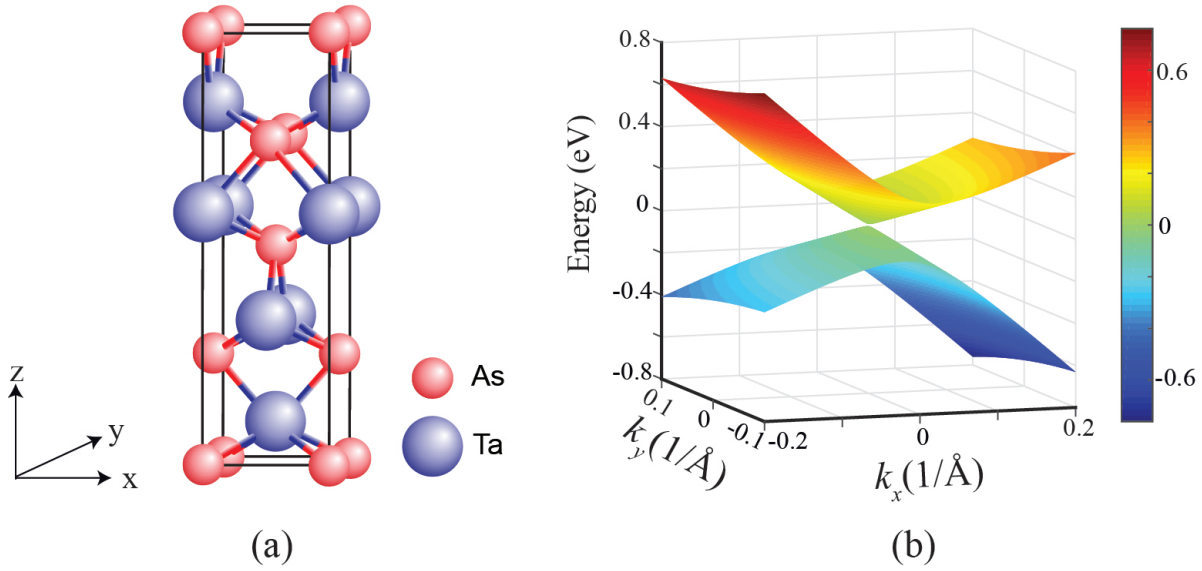

Figure 4.2 (Color online) (a) Body-centered tetragonal structure of TaAs. (b) Energy dispersion of TaAs near the second Weyl point.

Fig. 4.2 (b) as a function of k_x and k_y for $k_z = 0$. The reciprocal vector is measured relative to the Weyl point, i.e., the coordinates of the Weyl point are $(0, 0, 0)$. The parameters of the effective low-energy Hamiltonian (4.1) can be found from the known velocities in the conduction and valence bands [43; 44]. The corresponding parameters are shown in Table 1 for two sets of Weyl points. The study of dynamics of TaAs in ultrafast pulse reveals that after photoexcitation by a short pulse, their relaxation happens in a few-picoseconds [45] which make these materials to be a suitable candidate for optical switches. Here we study another aspect of dynamics of these materials in an ultrafast optical pulse. Below we consider different directions of pulse polarization. We describe the response of the system in terms of CB population and distribution of CB population in the reciprocal space. Such distribution is strongly correlated with the profile of the corresponding interband dipole matrix elements.

Table 4.1 The parameters (velocities) of effective Hamiltonian (4.1) in units of 10^5 m/s for two sets of Weyl points.

Velocity	W_1	W_2
v_{0x}	-1.35	-0.95
v_{0y}	-1	0.9
v_{0z}	0	1.35
v_x	3.85	3.35
v_y	2.2	2.6
v_z	0.2	2.95

4.3.1 Linearly-polarized pulse

4.3.1.1 x-polarized pulse

We apply the x-polarized pulse (the pulse is incident normally on the system along the z direction), see Figure 4.2 (a). The optical pulse has the following form

$$F(t) = F_0 e^{-(t/\tau)^2}(1 - 2(t/\tau)^2). \tag{4.16}$$

Here, τ is the duration of pulse and is set to 2 fs and $F_0 = 0.075$ (V/Å) is the amplitude of the pulse.

For x-polarized pulse, the coupling between the bands is determined by the x component of the interband dipole matrix element, D_x. For the first Weyl point, W_1, the interband dipole matrix elements D_x is shown as a function of the reciprocal vector, $\mathbf{k}$, in Figure 4.3. Considering the dipole matrix element as a function of k_x and k_y at a fixed value of k_z, we can characterize its behavior as follows. At $k_z = 0$, the dipole matrix element is singular at the Weyl point. This singularity is exactly of the same type as a singularity of the interband dipole matrix element in graphene. For nonzero k_z the system becomes similar to graphene with a gap. As a result, the dipole matrix element has two peaks (one is positive and another

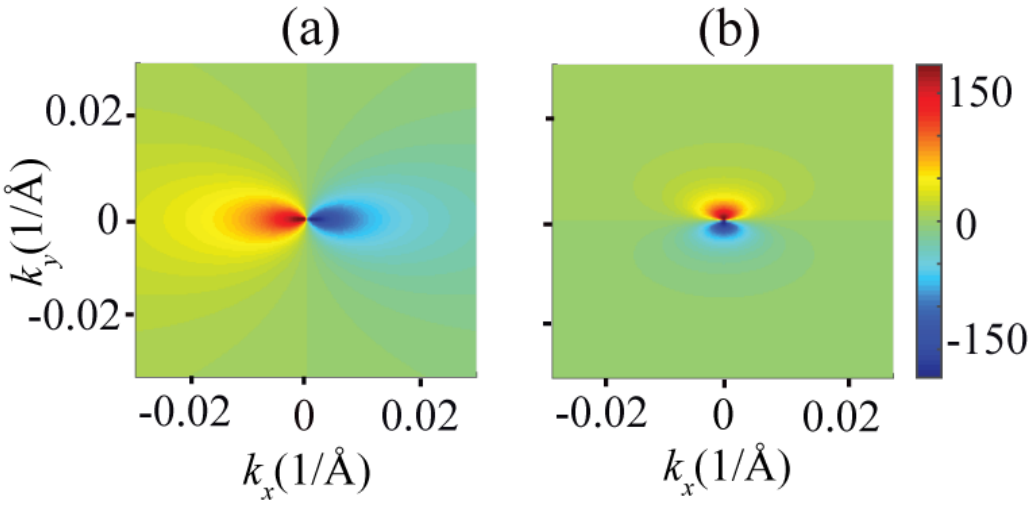

Figure 4.3 (Color online) Interband dipole matrix element D_x as a function of reciprocal vector $(k_x, k_y, 0.05)$ near the first Weyl point W_1. Both real (a) and imaginary (b) parts of D_x are shown.

is negative) near the origin (Weyl point). The corresponding distribution of the dipole matrix element is shown in Figure 4.3. For $k_z \neq 0$, the dipole matrix element has both real and imaginary parts.

Figure 4.4 shows the conduction band population near Weyl point W_1 as a function of reciprocal vector at different moments of time. The residual conduction band population has two peaks, the positions of which are correlated with the positions of the peaks of the dipole matrix element, D_x, shown in Figure 4.3. Initially, for $t < -1.5$ fs, the field accelerates the electrons to the left in Figure4.4. During this time the intensity of hot spots which indicates the population of conduction band near Weyl point is considerable, and this is because of the interband dipole coupling at this point is strong, and the most transfer from the valence band to the conduction band occurs near the Weyl point. After $t > -1.5$ fs the

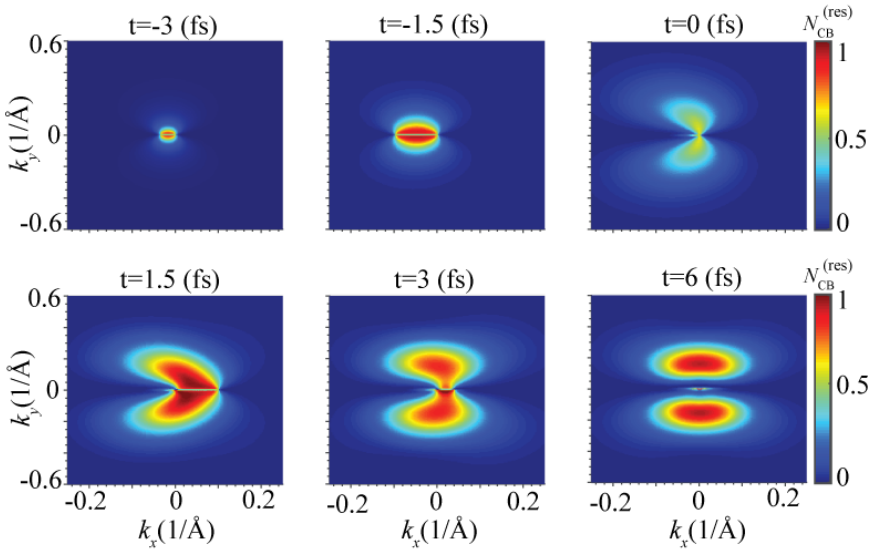

Figure 4.4 (Color online) Conduction band population as a function of wave vector near the first Weyl point, W_1, at different moments of time. The results are shown for x polarized pulse with the amplitude of $F_0 = 0.075$ (V/Å) and for $q_z = 0.05$ (1/Å).

field changes its sign, and as a result, the electrons move in the opposite direction and also undergo further VB to CB transitions. At $t = 0$ fs, the electrons return to the initial points, and continue to move in the same direction before the field changes its sign again at 1.5 fs and causes electrons to change the direction of their movement and return to the initial state at the end of the pulse. Passage the two times from the regime with large interband coupling causes interferences. Although during the pulse there is a large conduction band population near the origin (at moment of time $t = -1.5$ fs and 1.5 fs), at the end of the pulse, due to the destructive interference the conduction band population near the origin becomes almost zero. For the second set of Weyl points W_2, the CB population is illustrated in Figure4.5. The distribution of the CB population is the same as what we observed for the first set of Weyl points W_1 and the residual CB population is large near the Weyl point.

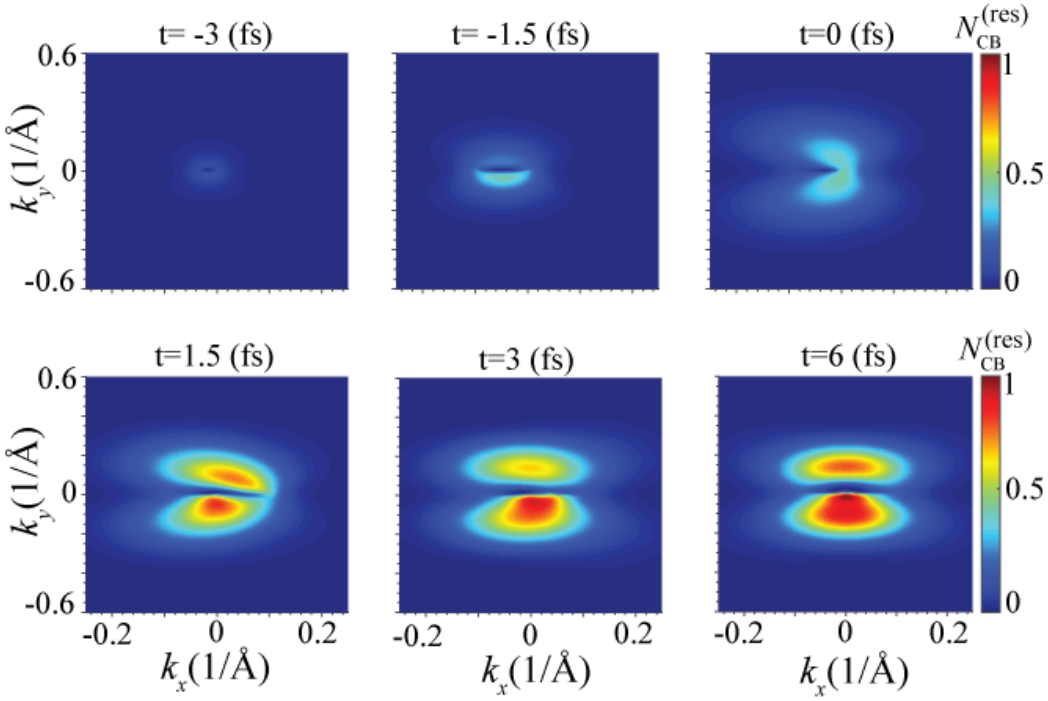

Figure 4.5 (Color online) Conduction band population as a function of wave vector near the second Weyl point, W_2, at different moments of time. The results are shown for x polarized pulse with the amplitude of $F_0 = 0.075$ (V/Å) and for $k_z = 0.05$ (1/Å).

4.3.1.2 y-polarized pulse

In this case, the light, Eq. (4.16), is incident normally on the system along the z direction, see Figure. 4.2(a). The profile of the dipole matrix element D_y as a function of the reciprocal vector is similar to the one of D_x. At $k_z = 0$, the dipole matrix element D_y as a function of k_x and k_y is singular at the Weyl point. At nonzero k_z, the dipole matrix element D_y has two peaks near the origin $[(k_x, k_y) = (0, 0)]$ - see Figure 4.6. The only difference between D_y and D_x is that D_y has a smaller magnitude, by $\approx 50\%$. The conduction band population

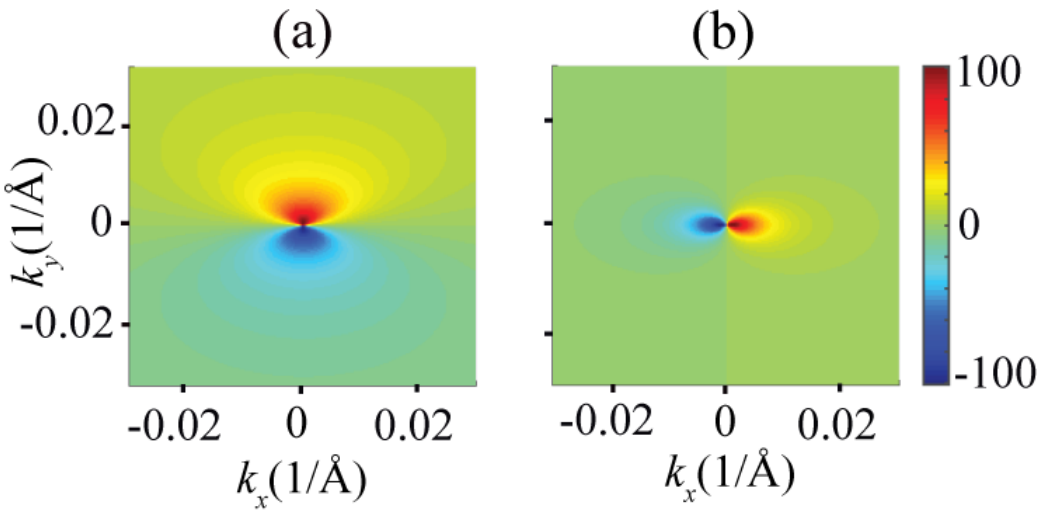

Figure 4.6 (Color online) Interband dipole matrix element D_y as a function of reciprocal vector $(k_x, k_y, 0.05)$ near the first Weyl point W_1. Both real (a) and imaginary (b) parts of D_y are shown.

distribution for the Weyl point W_1 is shown in Figure 4.7 at different moments of time. Similar to x-polarized pule, the residual conduction band population has two well-pronounced maxima, which are at the same positions as the maxima of the dipole matrix element, D_y. This behavior is similar to the one observed for x-polarized light. The main difference is that, the maximum residual conduction band population for y-polarized light is almost two times smaller than the maximum conduction band population for x-polarized light. This is due to a smaller value of the corresponding interband dipole matrix element. The distribution of hot spots which indicates the distribution of CB population in the momentum space for the second set of Weyl points in y-polarized pulse is shown in Figure4.8. Since the parameters (velocities) of the Hamiltonian in y direction, see Table.4.1, is similar for both sets of Weyl points, the pattern of the CB population for both sets of Weyl points is the same.

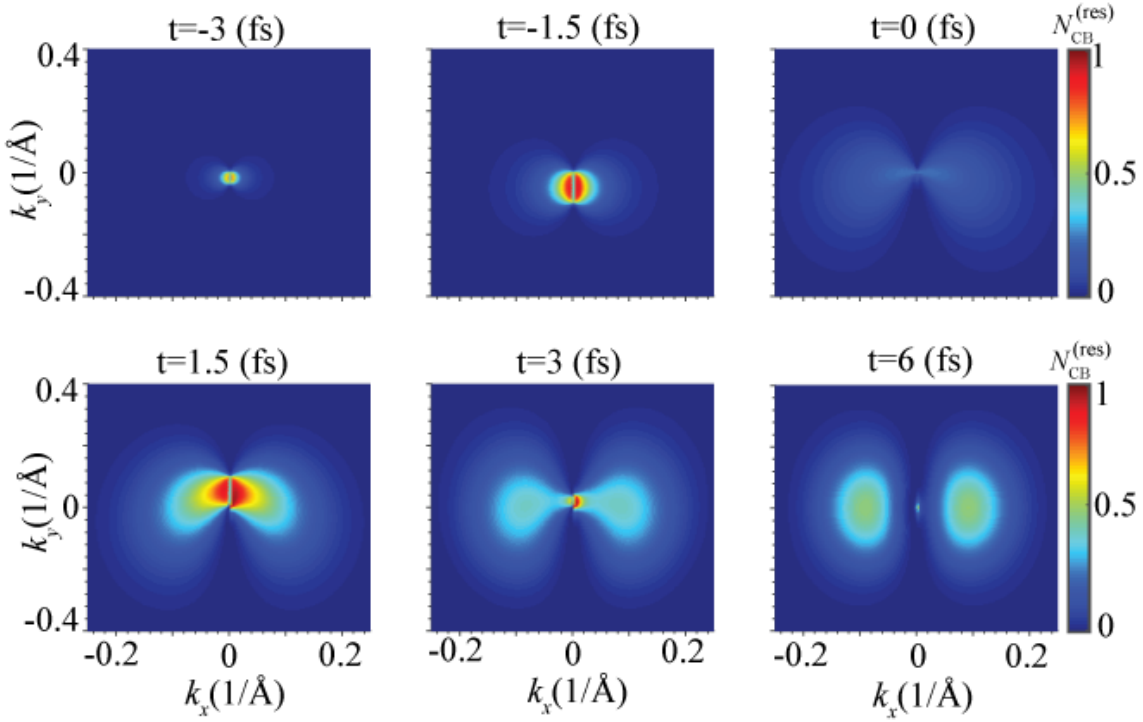

Figure 4.7 (Color online) Conduction band population as a function of wave vector near the first set of Weyl point, W_1, at different moments of time. The results are shown for y polarized pulse with the amplitude of $F_0 = 0.075$ (V/Å) and for $k_z = 0.05$ (1/Å).

4.3.1.3 z-polarized pulse

I this section, we apply the pulse, see Eq. (4.16), which is incident normally on the system along the y direction. The dependence of the interband dipole coupling on the reciprocal vector is determined by parameters of the effective Hamiltonian. The parameters of the Hamiltonian, corresponding to electron dynamics along x and y directions, are almost the same (see Table. 4.1), which results in similar response of the system to x and y polarized pulses. Along z direction, the corresponding parameters of the Hamiltonian (v_z and v_{0z}) are

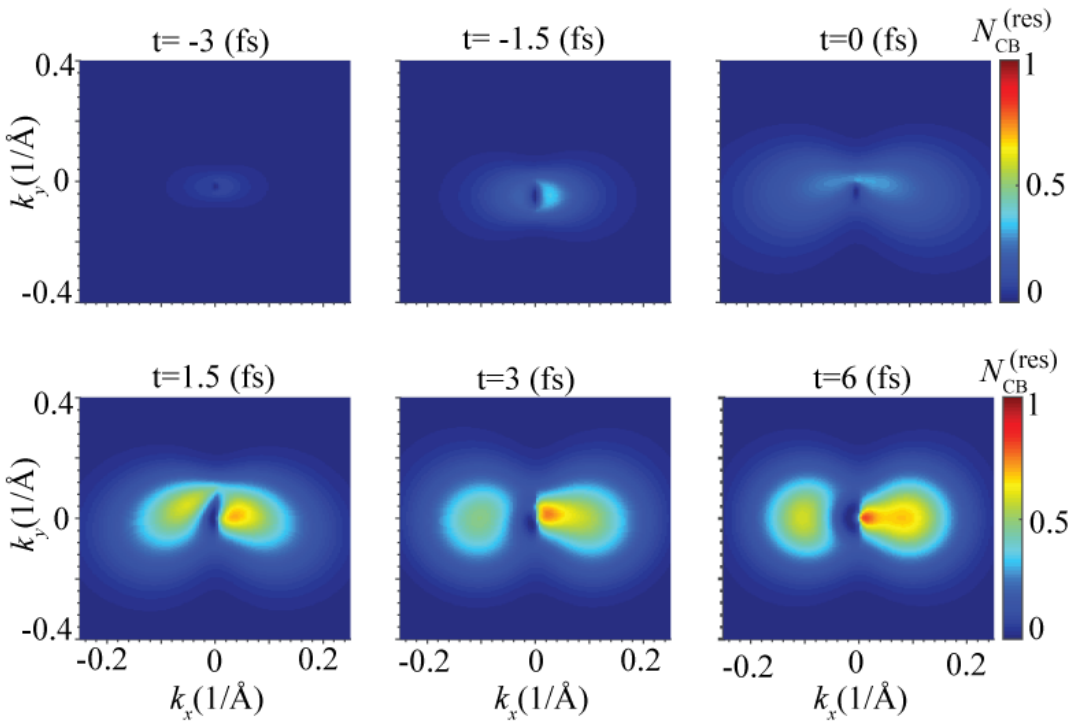

Figure 4.8 (Color online) Conduction band population as a function of wave vector near the second set of Weyl point, W_2, at different moments of time. The results are shown for y polarized pulse with the amplitude of $F_0 = 0.075$ (V/Å) and for $k_z = 0.05$ (1/Å).

small, which strongly modifies the dipole matrix elements and the electron dynamics along z direction. The dipole matrix element D_z for the Weyl point W_1 is shown in Figure. 4.9. The dipole matrix element D_z has a maximum at the Weyl point. This behavior is different from D_x and D_y, which have two maxima near the Weyl point.

The conduction band population distribution in the reciprocal space is shown in Figure 4.10 for W_1 for the field amplitude of $F_0 = 0.075$ (V/Å). During the pulse, there is a large conduction band population near the Weyl point. Such large population is due to strong mixing of the valence and conduction band states when an electron passes the region of large

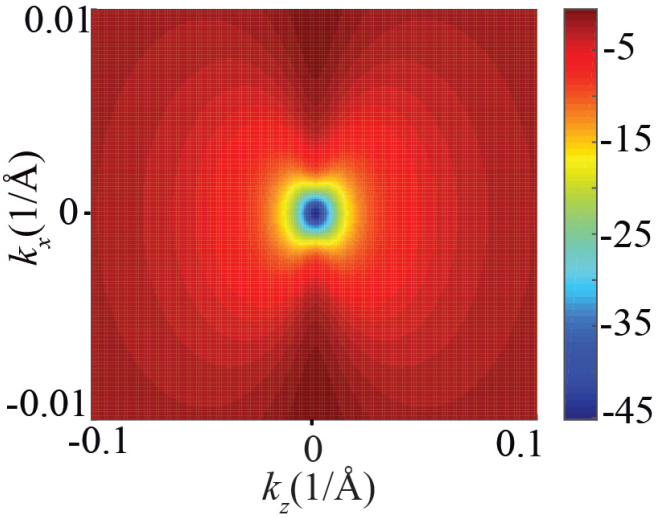

Figure 4.9 (Color online) Interband dipole matrix element D_z as a function of reciprocal vector $(k_x, 0, k_z)$ near the first Weyl point W_1. Only imaginary part of D_z is shown. The real part is zero.

interband coupling, which is near the Weyl point. The first passage of such region results in large conduction band population, while after the second passage the conduction band population becomes almost zero. Such cancellation of the conduction band population is the effect of destructive interference, which was also observed in graphene. Finally the residual conduction band population becomes almost zero. This is a unique feature of Weyl point W_1, which is due to highly localized nature of the interband dipole coupling near the Weyl point. The strength of localization of the dipole matrix element depends on the corresponding parameters of the Hamiltonian. For Weyl point W_2, which has order of magnitude larger velocities v_z and v_{0z} (see Table. 4.1), the residual conduction band population is relatively large and has two maxima near the Weyl point - see Figure. 4.11. Such conduction band population distribution is similar to the one for x and y- polarized light.

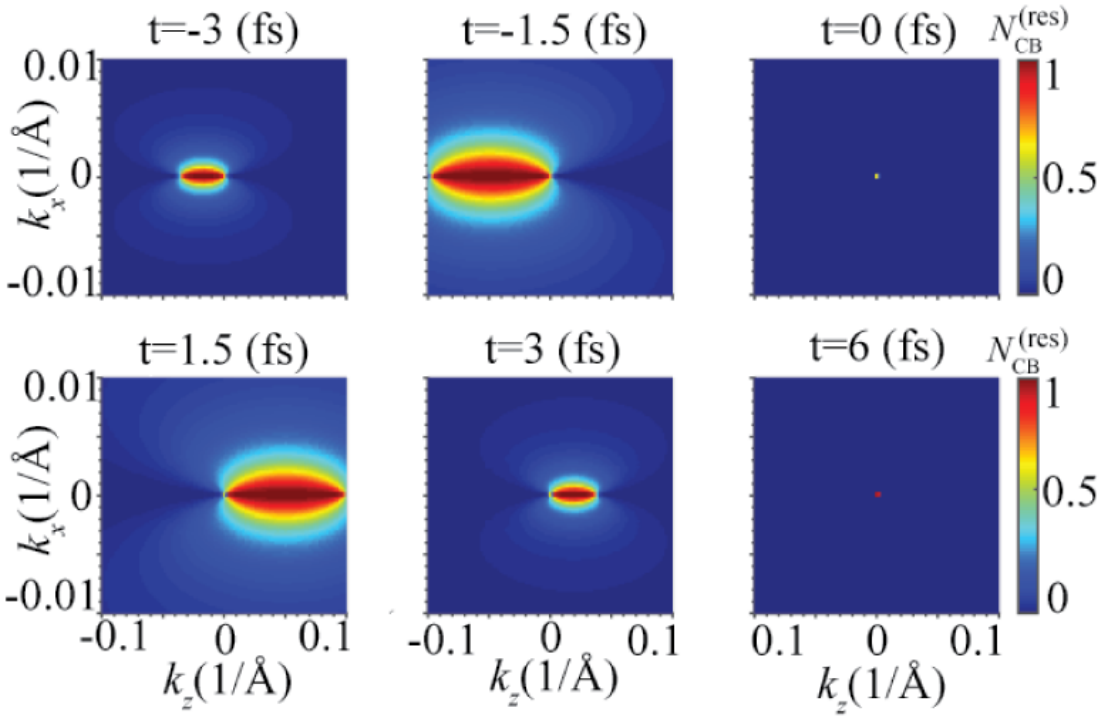

Figure 4.10 (Color online) Conduction band population as a function of wave vector near the first Weyl point, W_1, at different moments of time. The results are shown for z polarized pulse with the amplitude of $F_0 = 0.075$ (V/Å) and for $k_y = 0$ (1/Å).

4.3.1.4 Total occupation of the conduction band

Another important characteristic of electron dynamics in the field of the pulse is the total population of the conduction band, $\mathcal{N}_{CB}(t)$, see Eq.(2.11). Such conduction band population as a function of time is shown in Figure 4.12 for Weyl point W_1 and different pulse amplitudes. For x and y polarized pulses the electron dynamics is highly irreversible, which means that the residual conduction band population is comparable to the maximum conduction band population during the pulse, see Figure 4.12(a,b). Such irreversible dynamics is similar to the electron dynamics in two dimensional (2D) materials such as graphene and phosphorene

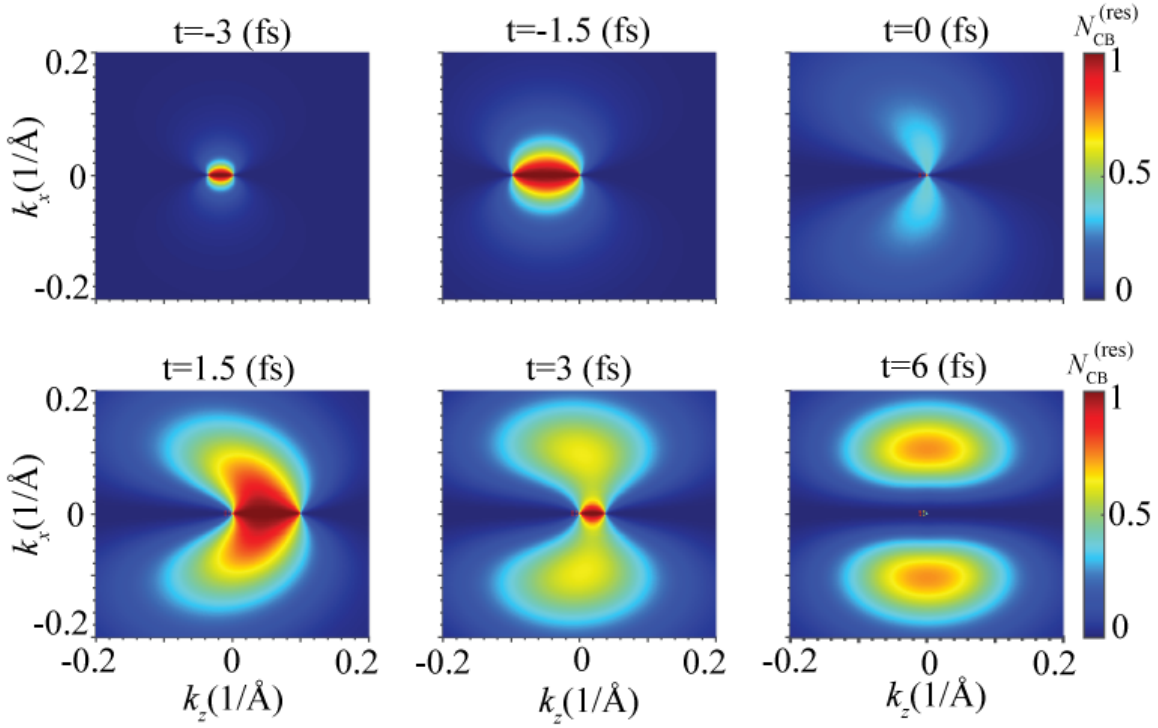

Figure 4.11 (Color online) Conduction band population as a function of wave vector near the second Weyl point, W_2, at different moments of time. The results are shown for z polarized pulse with the amplitude of $F_0 = 0.075$ (V/Å) and for $k_y = 0$ (1/Å).

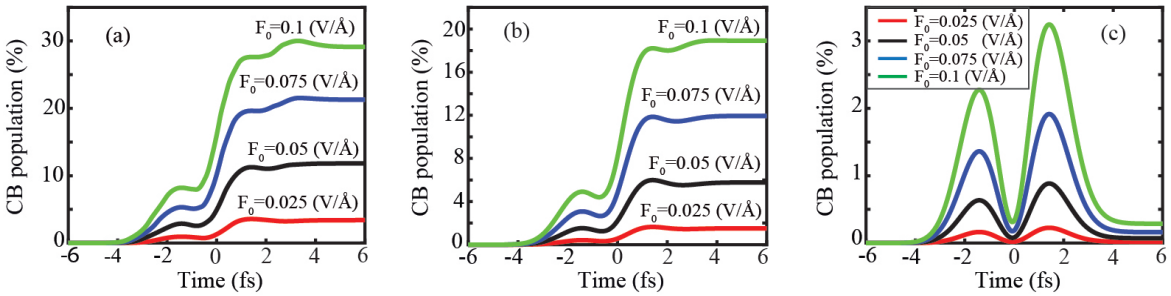

Figure 4.12 (Color online) Total conduction band population as a function of time for the first Weyl point, W_1. The pulse is polarized along (a) x (b) y (c) z directions.

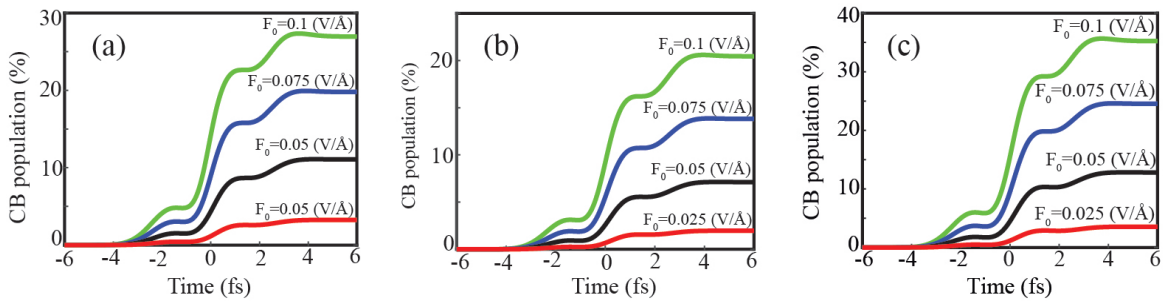

Figure 4.13 (Color online) Total conduction band population as a function of time for the second set of Weyl points, W_2. The pulse is polarized along (a) x (b) y (c) z directions.

[3; 4]. For z-polarized pulse the behavior is completely different, see Figure 4.12(c). The electron dynamics in this case is highly reversible - the residual conduction band population is almost zero, which means that the system returns to its initial state. During the pulse, the conduction band population is relatively large. In all cases (x, y, and z polarized pulses) the conduction band population monotonically increases with pulse amplitude.

For the second Weyl point, W_2, the electron dynamics for the x and y polarized pulses is similar to the one for the first Weyl point, W_1. The electron dynamics is irreversible and the residual conduction band population is comparable to the maximum conduction band population during the pulse. However, for z polarized pulse, the electron dynamics for Weyl point W_2 is completely different from the electron dynamics for Weyl point W_1. For z polarized pulse, the electron dynamics becomes highly irreversible - see Figure. 4.13 (c). The residual conduction band populations, $N_x^{(res)}$, $N_y^{(res)}$, and $N_z^{(res)}$, for the first Weyl point, W_1 are shown in Figure 4.14 as a function of the pulse amplitude. The residual conduction band population for z polarized pulse is almost zero for all values of F_0, which illustrates reversibility of electron dynamics along z direction. For the x and y polarized pulses the

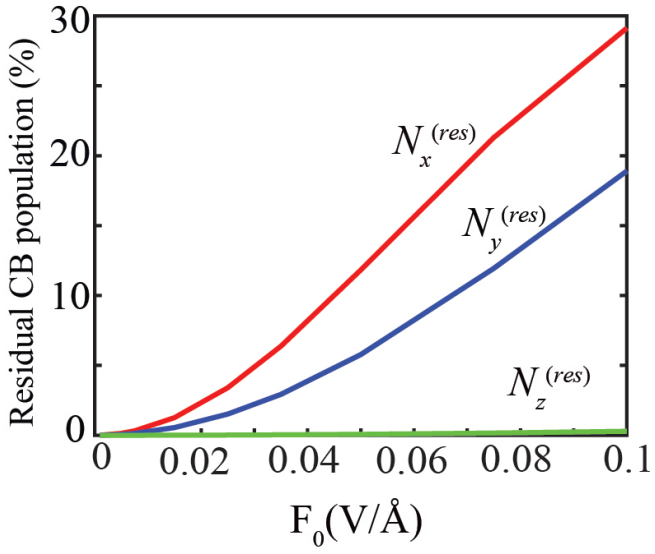

Figure 4.14 (Color online) Residual conduction band population as a function of pulse amplitude, F_0, for the first Weyl point, W_1. The results are shown for the x polarized ($N_x^{(res)}$), y polarized ($N_y^{(res)}$), and z polarized ($N_z^{(res)}$) pulses.

residual conduction band population monotonically increases with F_0.

4.3.1.5 Transferred charge

Interband electron dynamics results in redistribution of electrons between the valence and conduction bands, while intraband dynamics determines the transport of electrons within a single band. Combination of these two types of dynamics results in generation of electric current, which can be found from Eq. (2.12). The current as a function of time is shown in Figure 4.15. The current itself has two contributions: interband and intraband. Our results show that the electric current is mainly determined by the intraband contribution. This can be also seen in Figure 4.15, where both the current and the vector potential are shown. The results show that the current follows the vector potential. As we discussed before, the in-

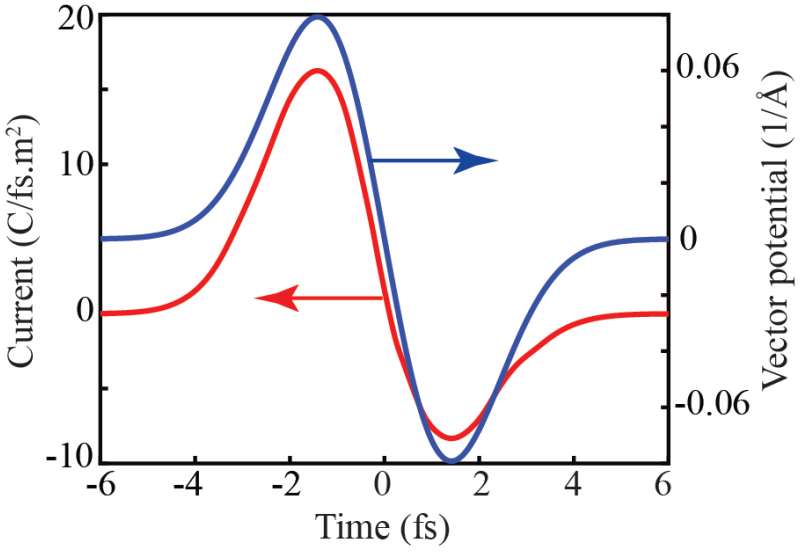

Figure 4.15 (Color online) Current and vector potential , $\int F(t)dt$, as a function of time for x polarized pulse with the amplitude of $F_0 = 0.08$ (V/Å). The results are shown for the first Weyl point, W_1.

traband electron dynamics is determined by the acceleration theorem and the corresponding electron momentum follows the vector potential. Since the total current, shown in Figure 4.15, follows the vector potential, then we can conclude that the total current is mainly determined by the intraband contribution. This is valid for all directions of pulse polarization.

With the known electric current, the charge transferred through the system can be calculated as an area under the current versus time graph. The transferred charge as a function of field amplitude, F_0, is shown in Figure 4.16 for both set of Weyl points. Here Q_x, Q_y and Q_z correspond to x, y and z polarized pulses, respectively. For the first Weyl point, W_1, for z polarized pulse, the transferred charge is almost zero but the transferred charges Q_x and Q_y monotonically increase with the field amplitude. The transferred charge for y polarized pulse is almost five times smaller than the transferred charge for x polarized pulse. In all

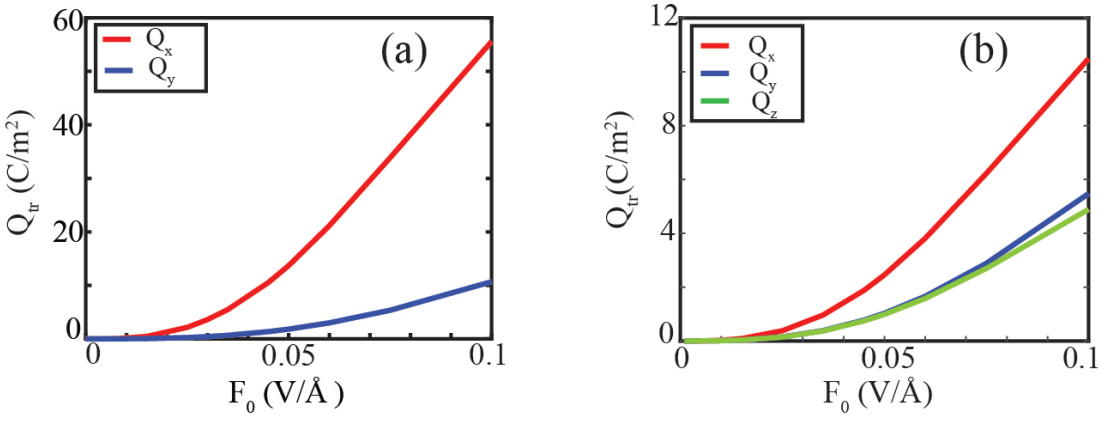

Figure 4.16 (Color online) Transferred charge through Weyl semimetal as a function of pulse amplitude for (a) the first Weyl point, W_1 and (b) the second Weyl point W_2. The results are shown for x polarized and y polarized and z polarized pulses.

cases, the transferred charge is positive, which means that the direction of the transfer is the same as the direction of the field maximum. For the second Weyl point, the transferred charge for z polarized pulse is nonzero and is almost equal to the transferred charge for y polarized pulse. For all directions of polarization, the transferred charge is positive and monotonically increases with field. The data also show that the transferred charges Q_x and Q_y for Weyl point W_2 is less than the corresponding charges for Weyl point W_1. At small field amplitudes, the transferred charge is proportional to F_0^3.

Charge transfer as a function of angle between the pulse and x axis is shown in Figure 4.17 for the first Weyl point. Here we consider that the direction of pulse is fixed and the sample is rotating around the z axis. The data shows that charge transfer component in x direction, Q_x, is maximum at $\theta = 0$ and by increasing the angle, it decreases sharply to zero at $\theta = 90$. At this point the charge transfer changes its sign and increases to its maximum

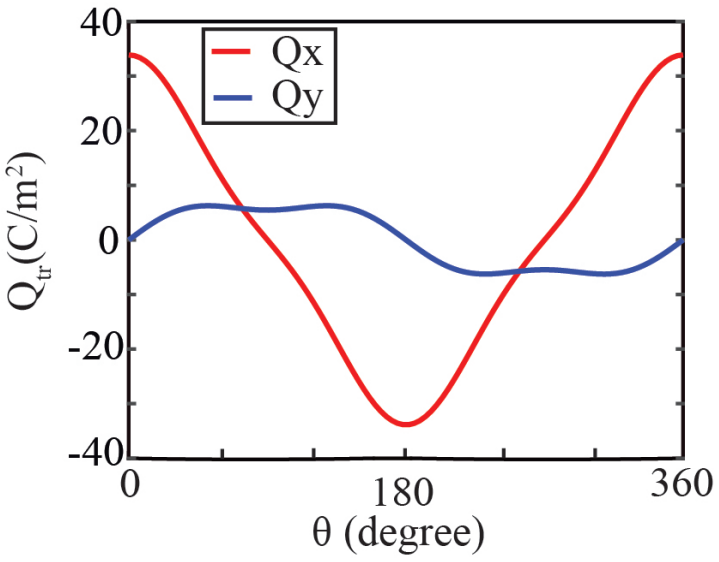

Figure 4.17 (Color online) Charge transfer as a function of angle between pulse and the x axis for $F_0 = 0.075$ (V/Å) for W_1

value in negative direction at $\theta = 180$ and then reverse itself and returns to its maximum value at $\theta = 360$. As we expected, the charge transfer in y direction, Q_y, is zero when the pulse is totally in x direction. But, by increasing the angle, Q_y rises slightly and achieves to its peak at $\theta = 45$. Then it deeps slightly before it returns to its peak again at $\theta = 135$ and after that it repeats its behavior but in negative direction.

4.3.1.6 Conclusion

The Weyl semimetals have zero bandgap, which suggests that a femtosecond dynamics of electrons in such materials should be highly irreversible, i.e., the residual electron population after the pulse is comparable to the conduction band population during the pulse. Such dynamics has been observed in graphene, which is a 2D version of Weyl semimetals. Our results show that the ultrafast electron dynamics is determined by not only the bandgap of

the material but also by the profile and the magnitude of the interband dipole elements. We considered the case of TaAs Weyl semimetal, which has two sets of Weyl points. We found that for the first set of Weyl points, the electron dynamics is highly anisotropic. Namely, while for x and y polarized optical pulses the electron dynamics is irreversible, for z polarized optical pulse the electron dynamics is highly reversible. For z polarized optical pulse, the residual conduction band population is almost zero after the pulse. Such high reversibility is due to relatively small value of z component of interband dipole matrix element and its high localization near the Weyl point.

For the second set of Weyl point, the electron dynamics is irreversible for all directions of polarization of the optical pulse. In all cases, the residual conduction band population is comparable to the maximum conduction band population. The femtosecond optical pulse also causes the charge transfer through the system during the pulse. The magnitude of the charge transfer strongly depends on the direction of polarization. For the first set of Weyl points, for z polarized pulse, the transferred charge is almost zero. For x and y polarized pulses the charge is transferred in the direction of the pulse maximum. The magnitude of the transferred charge for x polarized pulse is almost five times larger than the magnitude of the transferred charge for y polarized pulse.

For the second set of Weyl points, the charge is transferred through the system for all directions of polarization. Similar to the first set of Weyl points, the maximum charge is transferred for x polarized optical pulse.

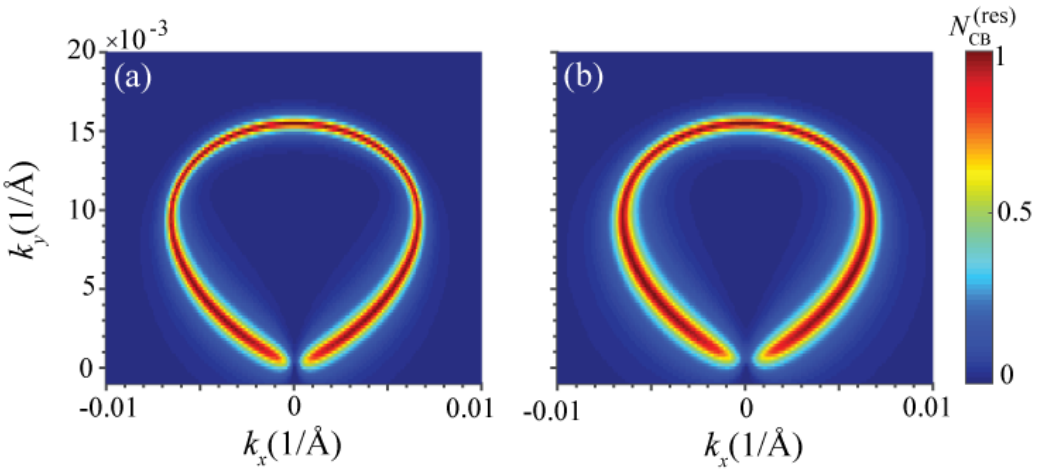

Figure 4.18 (Color online) Residual CB population, as a function of k_x and k_y in the reciprocal space for (a) the first set of Weyl points at $k_z = 0.01$ 1/Å (b) the second set of Weyl points at $k_z = 0.001$ 1/Å. The amplitude of the circularly-polarized optical field is $F_0 = 0.01$ V/Å.

4.3.2 Circularly-polarized pulse

We assume that a circularly-polarized pulse with the duration of $\tau = 1$ (fs) propagates in the z direction on a Weyl semimetal and has the following form

$$F_x(t) = F_0 e^{-(t/\tau)^2}(1 - 2(t/\tau)^2), \tag{4.17}$$

$$F_y(t) = 2F_0 e^{-(t/\tau)^2}(t/\tau), \tag{4.18}$$

where $F_0 = 0.01$ (V/Å) is pulse amplitude. Such a pulse induces a finite conduction band (CB) population in the reciprocal space. The residual CB population for both sets of Weyl

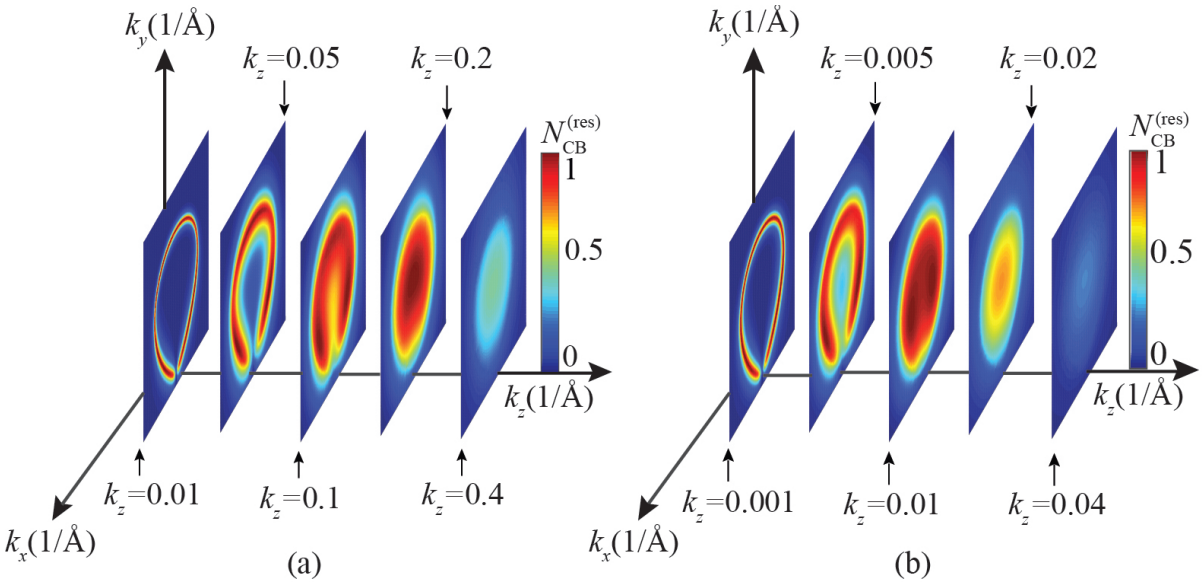

Figure 4.19 (Color online) Residual CB population, as a function of **k** in reciprocal space for (a) the first set of Weyl points and (b) second set of Weyl points after circularly-polarized pulse. The amplitude of the optical field is $F_0 = 0.01$ V/Å

points at a specific k_z is illustrated in Figure4.18. Also, Figures 4.19 (a) and (b) show the electron population of conduction band in $x-y$ plane in the momentum space for different values of k_z for the first and second Weyl point, respectively. The results show that the electron dynamics for such materials is coherent and highly irreversible, i.e., the residual conduction band (CB) population is comparable to the maximum CB population during the pulse. For both Weyl points the largest CB population is located near the Weyl points and along the separatrix which is defined as a set of the initial points for which electron trajectories in the reciprocal space pass precisely through $(k_x, k_y) = (0, 0)$ point. In fact, the separatrix is a $x-z$ mirror reflection of electron trajectory originating at the $(k_x, k_y) = (0, 0)$ point. In order to explain the distribution of CB population in reciprocal space we need to consider the characteristics of dipole matrix elements as a function of k_x and k_y at a fix

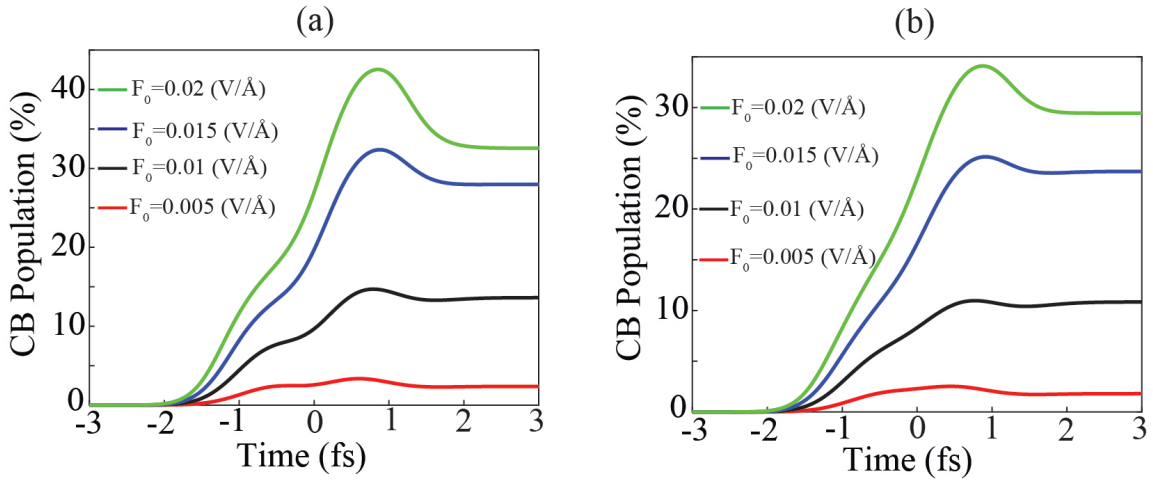

Figure 4.20 (Color online) The electron population of the conduction band for (a) the first and (b) second set of Weyl points, as a function of time for different amplitude of field.

value of k_z. For small k_z, the dipole matrix element is highly localized near $(k_x, k_y) = (0, 0)$ point which results the maximum of electron transfer between valence band and conduction band in this vicinity. As a result, the intensity of hot spots in the reciprocal space which indicates CB population, has sharp maximum along the separatrix. However, for large k_z the system behave similar to gapped graphene with delocalized interband coupling and the transfer of electrons between the valence band and the conduction bands are not confined within a narrow region. The pattern for both sets of Weyl points are the same. However, the value of k_z for the first and the second sets of Weyl points are different which is related to different parameters (velocities) of Hamiltonian at two sets of Weyl points. Figure 4.20 show the total occupation of the conduction band , $\mathcal{N}_{\mathbf{CB}}(t)$, as a function of time for different amplitude of fields for both sets of Weyl points. The data illustrates that the electron dynamics is highly irreversible, which means that the conduction band population at the end

of the pulse is large and is comparable to the maximum conduction band population during the pulse. The residual CB population for both cases are in the same order of magnitude and the population increase as the field become larger.

The optical pulse causes both interband and intraband electron dynamics in a system. Interband electron dynamics causes redistribution of electron between the valence and the conduction bands and intraband electron dynamics describes the motion of electron within a band. The combination of both electron dynamics causes electric current , Eq. (2.12), through the system during the pulse. The induced charge transfer can be obtained as an integral of the current, see Eq.2.13. Figures 4.21 (a) and (b) illustrate that for both sets of Weyl points charge transfer in all directions is negative and the magnitude of ,Q_x, is smaller than Q_y. For the first set of Weyl points, for small field, Q_x is almost zero and then it monotonically increases to almost 0.06 C/m^2 at $F_0 = 0.02$ V/Å. For the second set of Weyl points, Q_x is almost zero at up to $F_0 = 0.008$ V/Å and then increases slightly with the field amplitude. For the charge transfer in y direction, Q_y, for both sets of Weyl points there is almost a linear relationship between the field and the charge transfer up to 0.014 V/Å and the charge transfer increases with the field amplitude.

4.3.2.1 Conclusion

We have demonstrated that the electron dynamics of Weyl semimetals in a circularly-polarized pulse is highly irreversible which means the CB population of electron at the end of the pulse is large and is comparable to the maximum CB population during the pulse, and this behavior is similar to 2D materials such as graphene and phosphorene. The distri-

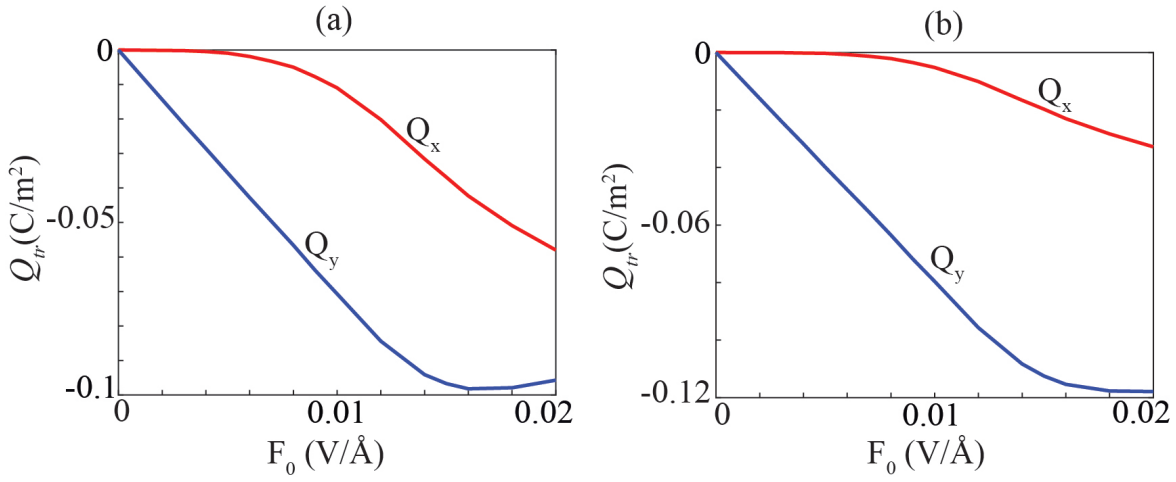

Figure 4.21 (Color online) Transferred charge density through TaAs as a function of F_0 for the (a) first and (b) second set of Weyl points. Q_x and Q_y denote to charge transfer along x and y directions, respectively.

bution of the CB population in the reciprocal space strongly depends on the profile of the dipole matrix elements near the Weyl points.

For both sets of Weyl points the distribution of the CB population in the momentum space follow the same pattern. A circularly-polarized pulse causes an electron to circle in the momentum space along the closed trajectory. The interband electron dynamics is characterized by redistribution of electrons between the valence and the conduction bands. Such redistribution is mainly determined by both the profile and strength of the dipole matrix elements. The electron transition between the valence and the conduction bands occur predominantly in the vicinity of the Weyl points. At $k_z = 0$ the interband dipole matrix is singular at the Weyl points, $(0, 0, 0)$. The CB population in the reciprocal space is characterized by hot spots. For small k_z these hot spots are located near the Weyl points and along a thin separatrix, which is due to the fact that the interband coupling is highly localized in

this area. For nonzero k_z the system is similar to graphene with a gap and the interband dipole matrix is delocalized. Therefore, the transformation of electrons between the valence band and the conduction band are not confined in a narrow region.

The femtosecond single oscillation pulse also induces charge transfer in both x and y directions through the system during the pulse. For both sets of Weyl points, charge transfer in both x and y directions increase with the field.

CHAPTER 5

TOPOLOGICAL PROPERTIES OF WEYL SEMIMETALS IN ULTRAFAST OPTICAL PULSES: TOPOLOGICAL RESONANCE AND CHIRALITY

5.1 Introduction

Three-dimensional topological Weyl semimetals [43; 46–49] are characterized by linear band crossing called Weyl points. In 3D momentum space, a pair of Weyl points have opposite chirality, i.e., the Weyl points in a pair are sink or source of the Berry flux. In 3D, the observation of Weyl point requires the breaking of either time reversal symmetry T or inversion symmetry I. Nontrivial topological properties of Weyl semimetals in momentum space is due to the Berry curvature $\Omega(\mathbf{k})$. In 1984, Berry [50] reported that under adiabatic evolution, wave function of an electron state accumulates a geometric or Berry phase when encircle a loop in the momentum space. The Berry phase in the reciprocal space is similar to the Aharonov-Bohm [51] phase in the real space in the presence of a magnetic field. The Berry phase of the Bloch wave functions within a single band n is calculated by the line integral of the Berry connection $\mathbf{A}$. The Berry connection generates the corresponding Berry curvature, $\Omega(\mathbf{k})$, $\Omega(\mathbf{k}) = \nabla \times \mathbf{A}(\mathbf{k})$.

For a system with I symmetry, $\Omega(-\mathbf{k})$=$\Omega(\mathbf{k})$ and a Weyl point $\mathbf{k}$ maps to another Weyl point at $-\mathbf{k}$ with reversed chirality. Under T symmetry, $\mathbf{k}$ will be mapped to $-\mathbf{k}$ and at the same time reverse the k-space Berry curvature, $\Omega(-\mathbf{k})$=$-\Omega(\mathbf{k})$. Therefore, a Weyl point $\mathbf{k}$ under T is mapped to another Weyl point at $-\mathbf{k}$ with the same chirality. As a result, if the system posses both symmetries, the net Berry curvature field must vanish, and so there is

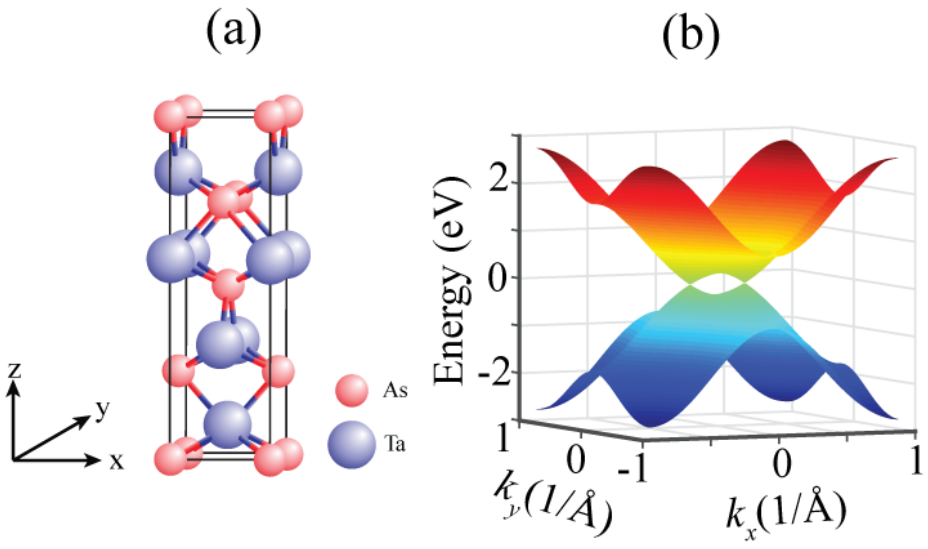

Figure 5.1 (Color online) Body-centered tetragonal crystal structure of TaAs. (b) Energy dispersion of TaAs near the Weyl points at $k_z = 0$.

no isolated Weyl points.

Due to the large Berry curvature, Weyl semimetals can have strong non-linear optical response to an external electric fields compared to the traditional electro-optic materials [52–56]. In this chapter, we theoretically study non-linear optical response of Weyl semimetal TaAs to linear and circularly polarized ultrafast pulses with a duration of a few femtoseconds. Such pulses cause topological resonance in Weyl semimetals which is due to strong Berry curvature which is localized at the Weyl points.

5.2 Model and main equations

In this study, we use a two-band Bloch model of Weyl semimetals [57]. Such Hamiltonian $\mathcal{H}_0$ describes the low-energy excitations near two Weyl's points located at $k_w^{\pm} = (\pm k_0, 0, 0)$

in the reciprocal space. The Hamiltonian has the following form

$$\mathcal{H}_0 = A(\mathbf{k})\sigma_x + B(\mathbf{k})\sigma_y + C(\mathbf{k})\sigma_z, \tag{5.1}$$

where $\mathbf{k} = (k_x, k_y, k_z)$ is a vector of the reciprocal space, σ_x, σ_y, σ_z are Pauli matrices, and $A(\mathbf{k})$, $B(\mathbf{k})$, $C(\mathbf{k})$ are given by the following expressions

$$A(\mathbf{k}) = \left[t_x * \Big(\cos(k_x a) - \cos(k_0 a) \Big) + t_y * \Big(\cos(k_y b) - 1 \Big) + t_z * \Big(\cos(k_z c) - 1 \Big) \right],$$

$$B(\mathbf{k}) = t_y * \sin(k_y b),$$

$$C(\mathbf{k}) = t_z * \sin(k_z c).$$

Here a, b and c are lattice constants along x, y and z directions, respectively, see Figure 5.1(a), and t_x, t_y, and t_z are hopping integrals which are related to the Fermi velocities v_x, v_y, and v_z at the Weyl's points through the following expressions

$$\begin{aligned} v_x &= -\Big(a/\hbar \Big) t_x \sin(\pm k_0 a), \\ v_y &= \Big(b/\hbar \Big) t_y, \\ v_z &= \Big(c/\hbar \Big) t_z, \end{aligned} \tag{5.2}$$

We apply our analysis to TaAs Weyl semimetal, which has a body-centered tetragonal lattice system, see Figure 5.1(a), with lattice constants $a = b = 3.437$ (Å) along x and y directions, respectively and $c = 11.646$ (Å) along z direction. TaAs has 24 Weyl points: eight

Weyl points are located at $(\pm 0.0072\pi/a, 0.4827\pi/b, 1.000\pi/c)$ and are called W_1 and sixteen Weyl points are located at $(\pm 0.0185\pi/a, 0.2831\pi/b, 0.6000\pi/c)$ and are called W_2 [49; 58]. The projections of all Weyl points on the $k_z = \pi/c$ plane are illustrated in Figure 5.3 (a). The two band Hamiltonian (5.1) is used to describe the electron dynamics near a pair of Weyl points, for example, a pair of Weyl points W_2, which are shown inside the dashed region in Figure 5.3 (a). With the known Hamiltonian (5.1), the corresponding energy for the valence band and the conduction band can be obtained as

$$E^v(\mathbf{k}) = -\sqrt{A(\mathbf{k})^2 + B(\mathbf{k})^2 + C(\mathbf{k})^2}, \tag{5.3}$$
$$E^c(\mathbf{k}) = +\sqrt{A(\mathbf{k})^2 + B(\mathbf{k})^2 + C(\mathbf{k})^2}.$$

The energy dispersion of TaAs near these Weyl points is shown in Figure 5.1 (b). Substituting the wave functions found from the field-free Hamiltonian (5.1) into Eq. (2.9), we obtain the following expressions for the dipole matrix elements

$$D_x(\mathbf{k}) = \frac{t_x a}{2i(A^2(\mathbf{k}) + B^2(\mathbf{k}) + C^2(\mathbf{k}))} * \frac{\sin(k_x a)}{\sqrt{A^2(\mathbf{k}) + B^2(\mathbf{k})}} * \left(A(\mathbf{k})C(\mathbf{k}) + iB(\mathbf{k})\sqrt{A^2(\mathbf{k}) + B^2(\mathbf{k}) + C^2(\mathbf{k})} \right), \tag{5.4}$$

$$D_y(\mathbf{k}) = \frac{t_y b}{2i(A^2(\mathbf{k}) + B^2(\mathbf{k}) + C^2(\mathbf{k}))} * \frac{1}{\sqrt{A^2(\mathbf{k}) + B^2(\mathbf{k})}} \Bigg(C(\mathbf{k}) \Bigg(A(\mathbf{k}) \sin(k_y b) - B(\mathbf{k}) \cos(k_y b) \Bigg) + i\sqrt{A^2(\mathbf{k}) + B^2(\mathbf{k}) + C^2(\mathbf{k})} \Bigg(A(\mathbf{k}) \cos(k_y b) + B(\mathbf{k}) \sin(k_y b) \Bigg) \Bigg), \tag{5.5}$$

$$D_z(\mathbf{k}) = \frac{t_z c}{2i(A^2(\mathbf{k}) + B^2(\mathbf{k}) + C^2(\mathbf{k}))} \sqrt{A^2(\mathbf{k}) + B^2(\mathbf{k})} * \Bigg(\frac{\sin(k_z c)}{A^2(\mathbf{k}) + B^2(\mathbf{k})} \Bigg(A(\mathbf{k})C(\mathbf{k}) + iB(\mathbf{k})\sqrt{(A^2(\mathbf{k}) + B^2(\mathbf{k}) + C^2(\mathbf{k})} \Bigg) + \cos(k_z c) \Bigg). \tag{5.6}$$

The matrix elements of the velocity operator, Eq. (2.10), calculated between the valence and the conduction band states have the following form

$$V_x^{vv} = -V_x^{cc} = \frac{t_x a A(\mathbf{k}) \sin(k_x a)}{\hbar\sqrt{A^2(\mathbf{k}) + B^2(\mathbf{k}) + C^2(\mathbf{k})}}, \tag{5.7}$$

$$V_x^{vc} = (V_x^{cv})^* = \frac{t_x a}{\hbar\sqrt{A^2(\mathbf{k}) + B^2(\mathbf{k}) + C^2(\mathbf{k})}} \frac{\sin(k_x a)}{\sqrt{A^2(\mathbf{k}) + B^2(\mathbf{k})}} * \Bigg(A(\mathbf{k})C(\mathbf{k}) - iB(\mathbf{k})\sqrt{A^2(\mathbf{k}) + B^2(\mathbf{k}) + C^2(\mathbf{k})} \Bigg), \tag{5.8}$$

$$V_y^{vv} = -V_y^{cc} = \frac{t_y b}{\hbar\sqrt{A^2(\mathbf{k}) + B^2(\mathbf{k}) + C^2(\mathbf{k})}} \times \Bigg(A(\mathbf{k}) \sin(k_y b) - B(\mathbf{k}) \cos(k_y b) \Bigg), \tag{5.9}$$

$$V_y^{vc} = (V_y^{cv})^* = \frac{t_y b}{\hbar\sqrt{A^2(\mathbf{k}) + B^2(\mathbf{k}) + C^2(\mathbf{k})}} \times \frac{1}{\sqrt{A^2(\mathbf{k}) + B^2(\mathbf{k})}} \Bigg(C(\mathbf{k}) \Bigg(A(\mathbf{k}) \sin(k_y b) - B(\mathbf{k}) \cos(k_y b) \Bigg) - i\sqrt{A^2(\mathbf{k}) + B^2(\mathbf{k}) + C^2(\mathbf{k})} \Bigg(A(\mathbf{k}) \cos(k_y b) + B(\mathbf{k}) \sin(k_y b) \Bigg) \Bigg), \tag{5.10}$$

$$V_z^{vv} = -V_z^{cc} = \frac{t_z c}{\hbar\sqrt{A^2(\mathbf{k}) + B^2(\mathbf{k}) + C^2(\mathbf{k})}} \times \Bigg(A(\mathbf{k}) \sin(k_z c) - B(\mathbf{k}) \cos(k_z c) \Bigg), \tag{5.11}$$

$$V_z^{vc} = (V_z^{cv})^* = \frac{t_z c}{\hbar} \frac{\sqrt{A^2(\mathbf{k}) + B^2(\mathbf{k})}}{\sqrt{A^2(\mathbf{k}) + B^2(\mathbf{k}) + C^2(\mathbf{k})}} \Bigg(\cos(k_z c) + \frac{\sin(k_z c)}{A^2(\mathbf{k}) + B^2(\mathbf{k})} \times \Bigg(A(\mathbf{k}) C(\mathbf{k}) - iB\sqrt{A^2(\mathbf{k}) + B^2(\mathbf{k}) + C^2(\mathbf{k})} \Bigg) \Bigg). \tag{5.12}$$

5.3 Results and discussions

5.3.1 Linearly polarized pulse

Below we report our results for the set of Weyl points W_2 with the positions of the Weyl points at $(\pm 0.0185\pi/a, 0, 0)$. The corresponding hopping integrals are $t_x = 10.90$, eV $t_y = 0.4917$, eV and $t_z = 0.1646$ eV.

We assume a linearly polarized pulse is incident normally on the sample along the z direction. The optical electric field has a following form

$$F_x(t) = F_0 e^{-u^2}(1 - 2u^2), \tag{5.13}$$

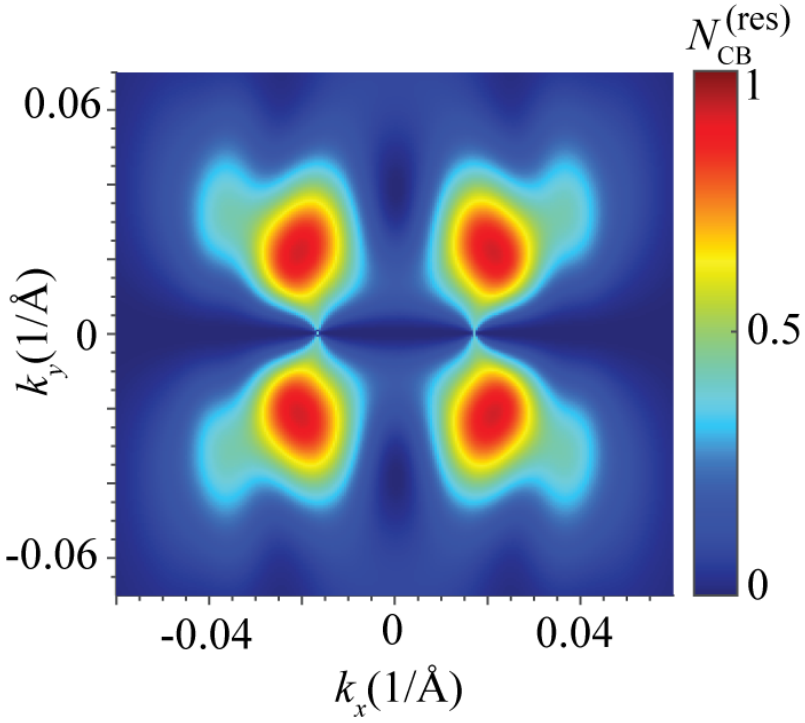

Figure 5.2 (Color online) Residual CB population as a function of (k_x, k_y) for $k_z = 0$. The pulse propagates along z direction. The field amplitude is $F_0 = 0.003$ V/Å.

where F_0 is field amplitude, $u = t/\tau$ and $\tau = 10$ fs is the duration of pulse. For such a pulse with this characteristics, the area under the pulse is always zero, i.e. $\int_{-\infty}^{\infty} F(t)dt = 0$.

For such polarization of the optical pulse the interband electron dynamics is determined by the x component of the interband dipole matrix element, D_x, which is shown in Figure 5.3 (b) at $k_z = 0$. The dipole matrix element is the largest near the Weyl's points.

We characterize the electron dynamics in the field of the pulse by the residual conduction band (CB) population distribution in the reciprocal space. The residual conduction band (CB) population for TaAs induced by a linearly polarized pulse with the field amplitude of 0.003 V/Å is shown in Figure 5.2. The data show that the large CB population is located

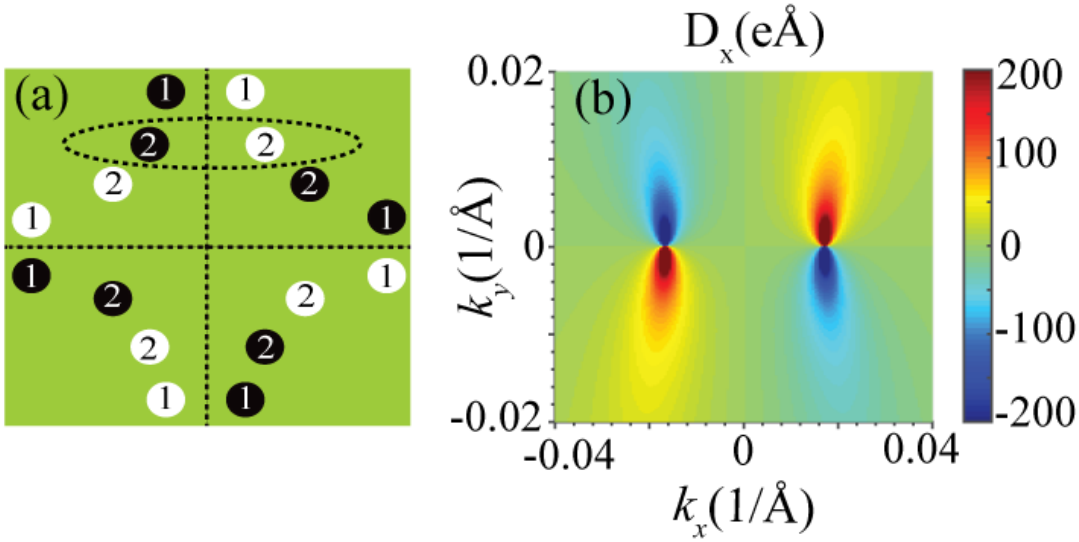

Figure 5.3 (Color online) (a) A projection of all Weyl's points on the $k_z = \pi/c$ plane. The four pairs of Weyl points, which are labeled by "1", are called W_1 and the other eight pairs of Weyl's points, which are labeled by "2", are called W_2. Black and white dots represent the opposite topological charges of the Weyl points. (b) Interband dipole matrix element, D_x as a function of reciprocal vector (k_x, k_y) for $k_z = 0$.

near the Weyl points. This is correlated with the profile of the interband dipole coupling, which is also the strongest near the Weyl points, see Figure 5.3 (b)

The CB population distribution is symmetric with respect to both x and y-axes, while the CB population is exactly zero along the line $k_x = 0$. This property is similar to what we have in graphene [4], and is due to singularity of D_x exactly at the Weyl's points or Dirac points for graphene.

Figure 5.4 shows the CB population of the system as a function of $\mathbf{k}$ at different moments of time. The applied pulse accelerates an electron with the initial crystal momentum to the left, $-30 < t < -7$ fs, then the field changes its sign and the electron moves to the right, at $-7 < t < 7$ fs. At $t = 7$ fs, the pulse changes its sign again and the electron returns to the initial position. The two passages of an electron through each given point results in

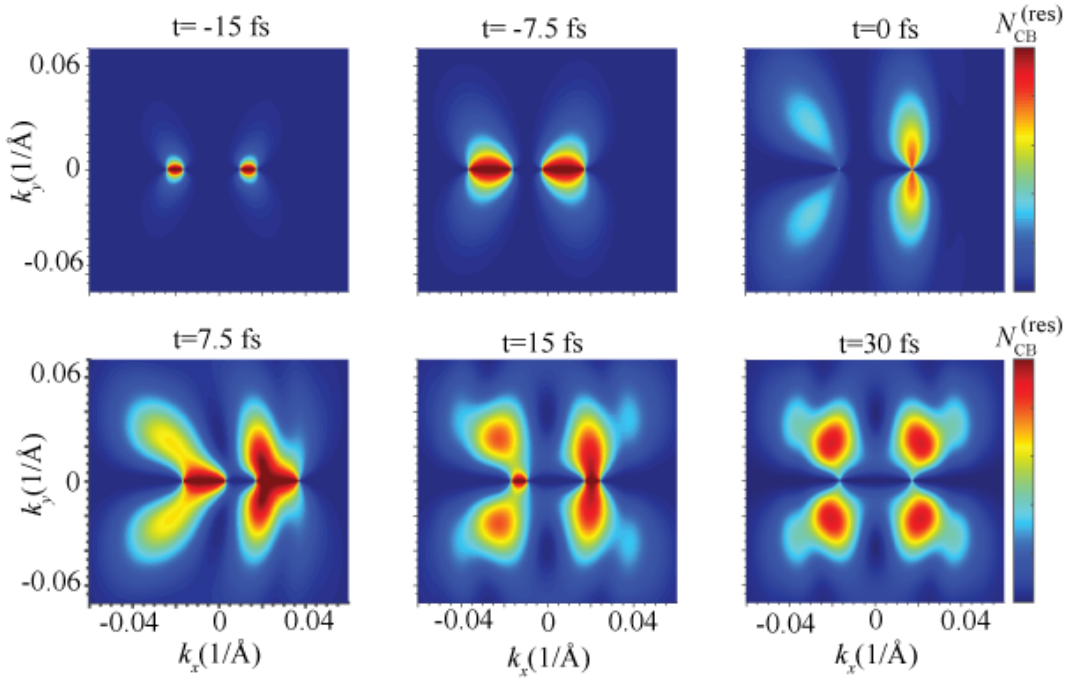

Figure 5.4 (Color online) The distribution of the CB population as a function of k_x, k_y for $k_z = 0$ at different moments of time. The field amplitude is $F_0 = 0.003$ V/Å

interference which manifests itself as hot spots in the reciprocal space.

For a non-zero value of k_z, the electron system in k_x-k_y plane near each Weyl's point becomes similar to gapped graphene. The corresponding CB population distribution as a function of k_x and k_y and for $k_z = \pm 0.03$ 1/Å is shown in Figure 5.5. The CB population distribution does not have any axial symmetries and the distributions above and below the Weyl's points are quite different. While for the left Weyl's point, the CB population has a maximum at $k_y > 0$, for the right Weyl's point, the CB population has a maximum at $k_y < 0$. This is quite different from the CB population distribution for $k_z = 0$ and is due

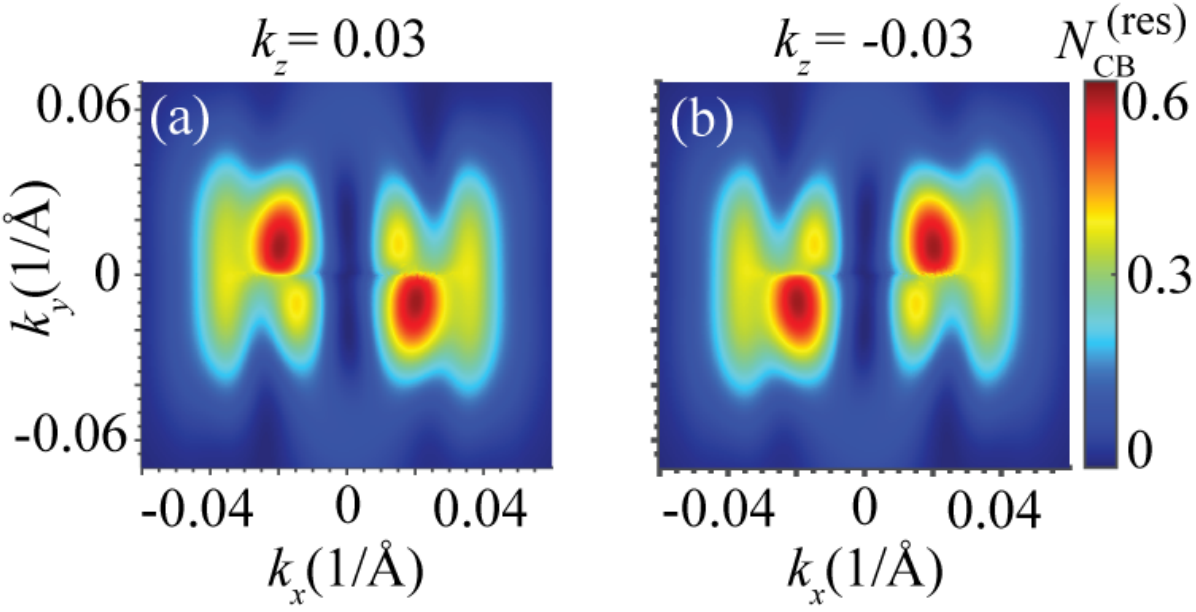

Figure 5.5 (Color online) Residual CB population, $N_{\rm CB}^{(\rm res)}(\mathbf{k})$, near the Weyl points for (a) $k_z = 0.03$ 1/Å. (b) $k_z = -0.03$ 1/Å. The amplitude of the optical field is $F_0 = 0.003$ V/Å.

to the fact that for $k_z \neq 0$, the effective 2D system (in $k_x - k_y$ plane) becomes similar to gapped graphene, for which there is the effect of topological resonance. The origin of the topological resonance can be understood by looking at the expression for the CB population in the first order of the perturbation theory.

In order to explain what we see in Figure 5.5 we need to introduce the following quantities,

$$\mathbf{A}'_{cv}(\mathbf{q},t) = \mathbf{A}_{cv}[\mathbf{k}(\mathbf{q},t)] \exp\left(i\phi_{cv}^{(d)}(\mathbf{q},t)\right), \tag{5.14}$$

$$\phi_{cv}^{(d)}(\mathbf{q},t) = -\frac{1}{\hbar}\int_{-\infty}^{t} dt_1 \left[E_c\Big(\mathbf{k}(\mathbf{q},t_1)\Big) - E_v\Big(\mathbf{k}(\mathbf{q},t_1)\Big)\right], \tag{5.15}$$

$$\boldsymbol{A}_{cv}(\mathbf{q}) = i\Big\langle \psi^{(c)}_{\mathbf{q}} | \nabla_{\mathbf{q}} \psi^{(v)}_{\mathbf{q}} \Big\rangle, \tag{5.16}$$

$$D_{cv}(\mathbf{q}) = e\mathbf{A}_{cv}(\mathbf{q}). \tag{5.17}$$

Here, c and v are the conduction and valence bands, respectively. $\phi^{(d)}_{cv}(\mathbf{q}, t)$ is a dynamic phase and matrix $\boldsymbol{A}_{\alpha'\alpha}(\mathbf{k})$ is the non-Abelian k-space gauge potential which is called Berry connection [50; 59].

In the Schrödinger representation, the dynamics of the system are described by the time-dependent wave function, $\psi(t)_S$ through the Schrödinger equation, Eq. (2.1). However, in many cases, it is more convenient to work in the interaction representation, expressed by

$$\psi(t)_I = e^{i\hat{H}_0 t/\hbar}\psi(t)_S. \tag{5.18}$$

In this representation, TDSE can be defined by

$$i\hbar\frac{\partial B_{\mathbf{q}}(t)}{\partial t} = H'(\mathbf{q}, t)B_{\mathbf{q}}(t), \tag{5.19}$$

where $B_{\mathbf{q}}(t)$ and Hamiltonian $H'(\mathbf{q}, t)$ are defined as

$$B_{\mathbf{q}}(t) = \begin{pmatrix} \beta_{v,\mathbf{q}}(t) \\ \beta_{c,\mathbf{q}}(t) \end{pmatrix}, \tag{5.20}$$

$$H'(\mathbf{q}, t) = e\mathbf{F}(t)\hat{\mathbf{A}}(\mathbf{q}, t), \tag{5.21}$$

$$\hat{\mathbf{A}}(\mathbf{q},t)=\begin{bmatrix}0 & \mathbf{A}'_{cv}(\mathbf{q},t)\\ \mathbf{A}'^{*}_{cv}(\mathbf{q},t) & 0\end{bmatrix}, \tag{5.22}$$

We numerically solve differential equation (5.19) with initial conditions $(\beta_{v\mathbf{q}},\beta_{c\mathbf{q}})=(1,0)$. A general solution can be expressed in terms of the evolution operator $\hat{U}(\mathbf{q},t)$ as

$$B_{\mathbf{q}}(t)=\hat{U}(\mathbf{q},t)B_{\mathbf{q}}(-\infty), \tag{5.23}$$

$$\hat{U}(\mathbf{q},t)=\hat{T}\exp\left[i\int_{t'=-\infty}^{t}\hat{\mathbf{A}}(\mathbf{q},t')d\mathbf{k}(\mathbf{q},t')\right], \tag{5.24}$$

where $\hat{T}$ denotes the time-ordering operator [60] and the integral is affected along the Bloch trajectory $\mathbf{k}(\mathbf{q},t)$ $\Big($Eq. (2.4)$\Big)$. At the end of the pulse the residual CB population is $N_{CB}^{(res)}(\mathbf{q})=N_{CB}(\mathbf{q},\infty)$.

To get a qualitative insight, consider Eq. (5.24) in the first order of perturbation theory, where it becomes

$$\hat{U}(\mathbf{q},t)=1+i\int_{t'=-\infty}^{t}\hat{\mathbf{A}}(\mathbf{q},t')d\mathbf{k}(\mathbf{q},t'). \tag{5.25}$$

The residual CB population correspondingly is

$$n_{\alpha}=\left|\oint\left|\mathbf{A}_{cv}[\mathbf{k}(\mathbf{q},t)]\mathbf{n}(t)\right|\exp\left(i\phi_{cv}^{(\mathrm{tot})}(\mathbf{q},t)\right)dk(\mathbf{q},t)\right|^{2}, \tag{5.26}$$

where $\mathbf{n}(t)=\mathbf{F}(t)/F(t)$ is the unit vector tangential to the Bloch trajectory and the total phase $\phi^{(\mathrm{tot})}$ is

$$\phi_{cv}^{(\mathrm{tot})}=\phi_{cv}^{(\mathrm{T})}(\mathbf{q},t)+\phi_{cv}^{(\mathrm{d})}(\mathbf{q},t), \tag{5.27}$$

and topological phase is defined as

$$\phi_{cv}^{(\mathrm{T})}(\mathbf{q},t) = \arg\Big(\mathbf{A}_{cv}(\mathbf{k}(\mathbf{q},t))\mathbf{n}(t)\Big). \tag{5.28}$$

Since $|\mathbf{A}_{cv}[\mathbf{k}(\mathbf{q},t)]\mathbf{n}(t)|$ is a smooth function of time, the residual CB population, Eq. (5.26), is determined by the oscillating phase factor $\exp[i\phi_{cv}^{(\mathrm{tot})}(\mathbf{q},t)]$. The phase consists of two parts: the dynamic phase and the topological phase, Eq.(5.27). The sum of these two contributions determines the magnitude of the CB population. If these two parts mutually cancel each other, then the accumulation of the CB population along the Bloch trajectory is large. Opposite, if the topological phase and the dynamic phase add together, then the total phase oscillates fast and the CB population is small. During the pulse, for all trajectories, the dynamic phase Eq. (5.15) decreases monotonically with time, t, and therefore the CB population is determined by how the topological phase changes with time. In Figure 5.6 we show the evolution of the topological phase along the electron trajectory in the reciprocal space for two different initial wave vectors: in one case the initial wave vector is above the Weyl's point, i.e., $k_y > 0$ - blue trajectory in Figure 5.6 (a), while in the other case the initial wave vector is below the Weyl's point, i.e., $k_y < 0$ - red trajectory in Figure 5.6 (a). For each trajectory, the electron passes through the region near the Weyl's point twice: first, when it moves in the positive direction of the x-axis and then when it moves in the negative direction of the x-axis. The corresponding topological phases as a function of time are shown in Figure 5.6 (b). Along each trajectory there are two large changes of the topological phase. These two changes correspond to two electron's passages of the Weyl's point. Since, at these two points, an electron moves in the opposite directions, the changes have opposite signs.

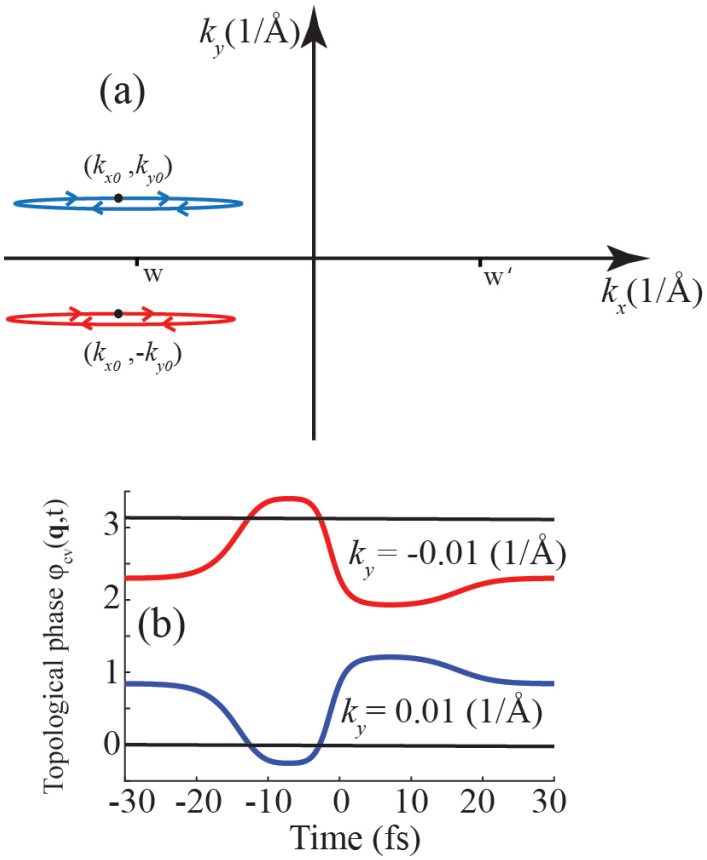

Figure 5.6 (Color online) Bloch trajectories, $\mathbf{k}(\mathbf{q},t)$, and the corresponding topological phases, $\phi_{cv}^{(T)}(\mathbf{q},t)$, are shown for two initial q-points during the pulse. (a) Electron Bloch trajectory $\mathbf{k}(\mathbf{q},t)$ in the reciprocal space is shown for initial point $(-0.019, 0.010, 0.030)$, by blue line, while the trajectory for initial point $(-0.019, -0.010, 0.030)$ is shown by red line. (b) Topological phases, $\phi_{cv}^{(T)}(\mathbf{q},t)$, along the corresponding Bloch trajectories from panel (a) are shown by blue and red lines. The black lines correspond to the topological phases along the trajectories with initial crystal momentum $(k_{x0}, -k_{y0}, 0)$ and $(k_{x0}, k_{y0}, 0)$.

Because the dynamic phase decreases with time, the topological resonance occurs only the topological phase increases with time, so the changes of these two phases cancel each other. Then, for the red trajectory, the topological resonance occurs at $t \approx -15$ fs, while for the blue trajectory, the topological resonance occurs at $t \approx 0$ fs.

The strength of the topological resonance depends on the magnitude of the electric field. Thus, while the topological resonance occurs for $k_y = 0.01$ V/Å(blue line in Figure 5.6(b)) at around $t \approx -15$ fs, it is not pronounced since the electric field at this moment is small. Therefore for $k_y = 0.01$ V/Å, i.e., below the left Weyl's point in Figure 5.6(a), the residual CB population is small. The topological resonance for $k_y = -0.01$ V/Å(red line in Figure 5.6(b)) occurs at $t \approx 0$ fs when the electric field is large. In this case the residual CB population is small for below the Weyl point. The topological resonances in the Weyl's semimetals occur because of the finite effective bandgap, Δ, which is determined by the finite value of k_z, $\Delta \propto k_z$. By changing the sign of k_z, we change the sign of the effective bandgap and, correspondingly, the sign of the topological phase - see Figure 5.7, where the topological phase is shown for both positive and negative values of k_z. As a results, while for positive k_z the topological resonance is realized at $k_y > 0$ for left Weyl's point and at $k_y < 0$ for right Weyl's point (see Figure 5.5 (a)), for negative k_z the topological resonance is realized at $k_y < 0$ for the left Weyl's point and at $k_y > 0$ for the right Weyl's point (see Figure 5.5 (b)). The residual CB population is completely centrosymmetric [61].

5.3.1.1 Conclusion

The topological resonance occurs in systems with nontrivial topology, such as gapped graphene, TMDC, Weyl's semimetals, and is due to competition between the topological phase and the dynamic phase. When these two phases cancel each other, the resonance occurs, which is visible as large CB population. In Weyl's semimetals, such resonance has been studied for circularly-polarized pulse [40] when an electron passes the Weyl's point only once, resulting

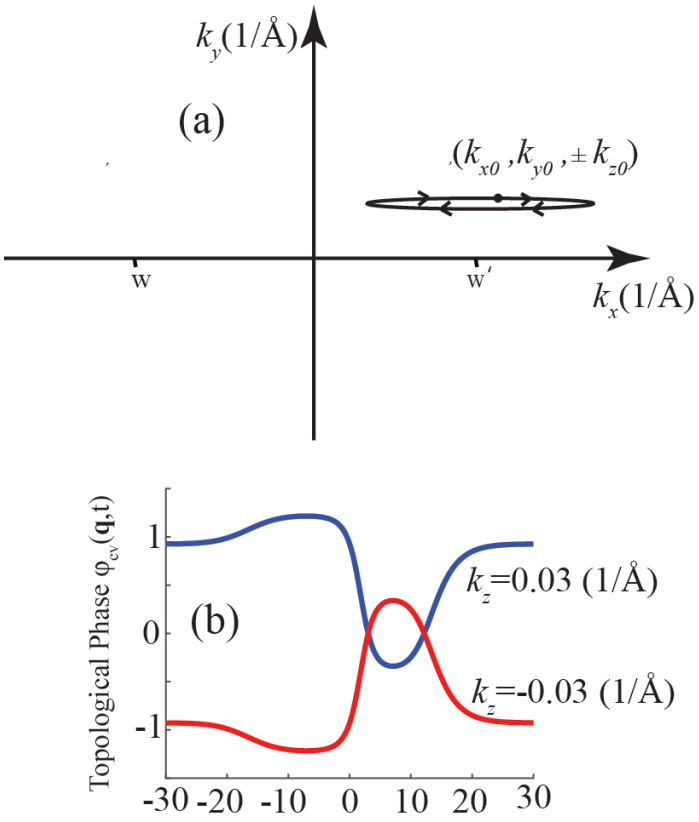

Figure 5.7 (Color online) Bloch trajectory $\mathbf{k}(\mathbf{q}, t)$ near the W point and the corresponding topological phases $\phi_{cv}^{(T)}(\mathbf{q}, t)$. (a) Electron Bloch trajectory $\mathbf{k}(\mathbf{q}, t)$ in the (k_x, k_y) plane is shown for initial points $(0.024, 0.011, \pm 0.030)$. (b) Topological phases $\phi_{cv}^{(T)}(\mathbf{q}, t)$ along the Bloch trajectory near the W point for initial wave vector $(0.024, 0.011, -0.030)$ is shown by red line, and for initial wave vector $(0.024, 0.011, +0.030)$ is shown by blue line.

in clear topological resonance for a given direction of passage. Here we report the topological resonance for linearly polarized pulse. Although, in this case, an electron passes the Weyl's point twice in opposite directions, the topological resonance occurs only when the electric field is large at the moment of passage. As a results, similar to a circularly polarized pulse, topological resonance can be observed for a linearly polarized pulse as an asymmetry distribution of the residual conduction band population in the reciprocal space.

5.3.2 Circularly polarized pulse

In this part of the study, in order to clearly observe phenomena, we assume that the position of the Weyl points are $(\pm 0.2, 0, 0)$.

5.3.2.1 Circularly polarized pulse with one single oscillation

We start this section by introducing the dipole matrix elements, $\mathbf{D}$, for TaAs. Dipole matrix elements are proportional to the Berry connection, see Eq. (5.16), $\mathbf{D}_{cv}(\mathbf{q}) = e\mathbf{A}_{cv}(\mathbf{q})$. The dipole matrix elements in the x direction, D_x and in the y direction, D_y as a function of k_x, k_y and for $k_z = 0$ are illustrated in Figure 5.8. The dipole coupling near the Weyl points is strong which results in the largest CB population near this area.

We assume a single oscillation right-handed circularly polarized (RCP) pulse which is incident normally on the system along the z direction, see Figure 5.1(a), with an amplitude $F_0 = 0.01$ V/Å.

$$F_x(t) = F_0 e^{-u^2}(1 - 2u^2), \qquad F_y(t) = 2uF_0 e^{-u^2}, \tag{5.29}$$

where $u = t/\tau$ and $\tau = 10$ fs. We numerically solve TDSE, Eq. (5.19), with the initial condition $(\beta_{v\mathbf{q}}, \beta_{c\mathbf{q}}) = (1, 0)$. An applied optical field causes transitions of electrons from the valence band to the conduction band resulting a finite CB population. The distribution of the residual conduction band population, $N_{\mathrm{CB}}^{(\mathrm{res})} = |\beta_{c\mathbf{q}}(t = \infty)|^2$, the CB population at the end of the pulse, as a function of $(k_x, k_y, 0)$, is illustrated in Figure 5.9.

We call the Weyl point at, $(-0.2, 0, 0)$ (1/Å) W and the Weyl point at $(0.2, 0, 0)$ (1/Å), W'.

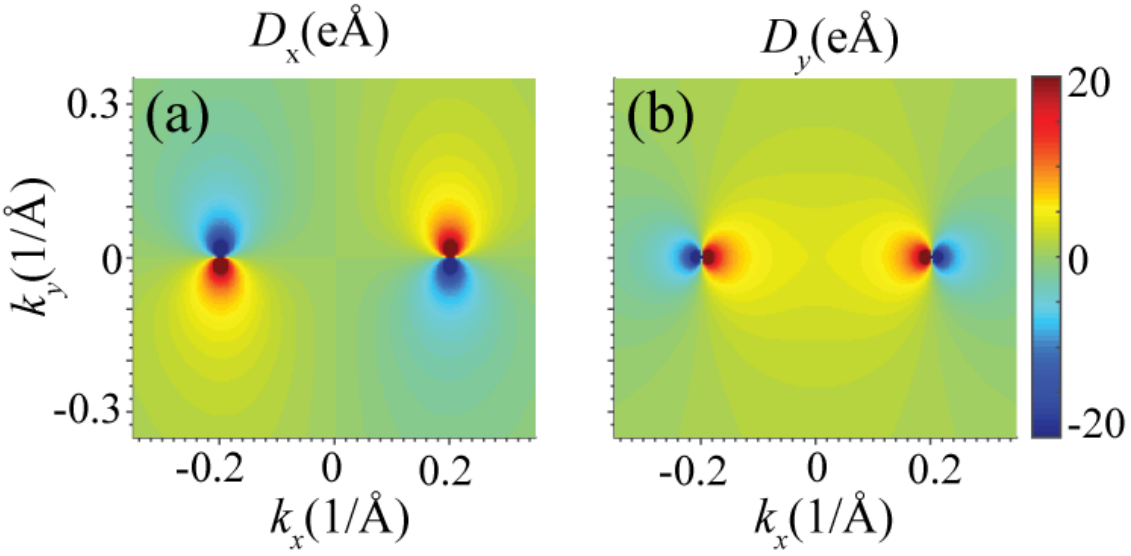

Figure 5.8 (Color online) Interband dipole matrix elements (a) D_x and (b) D_y as a function of reciprocal vector $(k_x, k_y, 0)$.

At $k_z = 0$, Figure 5.9, the response of both weyl points to an external electric field are similar which is the same as what we observed for graphene [5]. For graphene the response of both Dirac points, K and $K^{'}$, to the external electric field are similar. Since the interband dipole matrix elements are highly localized near the Weyl points, see Figure 5.8, the distribution of electrons has sharp maxima along the separatrix, both outside and inside. The separatrix, which is shown by a closed black line in Figure 5.11 (a) and (b), is a topological object which divides the momentum space into two regions. Any electron Bloch trajectory which originates inside the separatrix encircles the Weyl points, and if the Bloch trajectory originates outside the separatrix, it does not encircle the Weyl points. The data show that with an increase of k_z in positive direction, the W and $W^{'}$ become populated differently. For

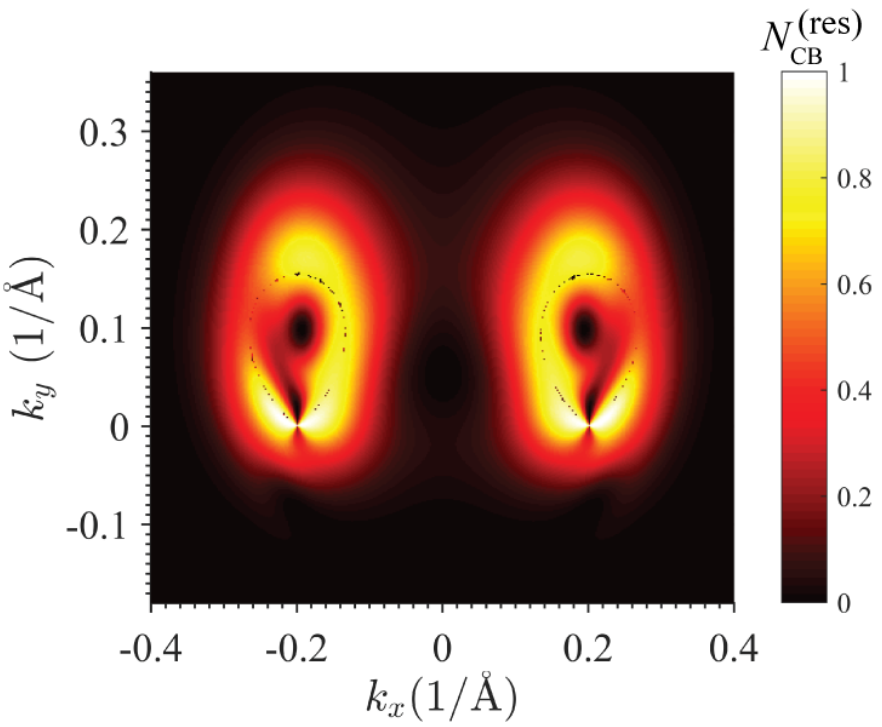

Figure 5.9 (Color online) Residual CB population as a function of (k_x, k_y) for $k_z = 0$ in reciprocal space after a single oscillation circularly polarized pulse. The pulse is incident normally on the system along the z direction. The amplitude of the pulse is $F_0 = 0.01$ V/Å

the W point, the major population occurs inside of the separatrix while the minor population occurs outside of the separatrix. In contrast, the large CB population is located outside the separatrix for $W^{'}$, Figure 5.10.

In order to explain the data, we return to Eq. (5.26). Since non-Abelian Berry connection element $\mathcal{A}_{cv}(\mathbf{k}(\mathbf{q},t))$ and topological phase $\phi_{cv}^{(\mathrm{T})}(\mathbf{q},t)$ are not gauge invariant, they are not observable. However, the CB population n_α is observable. Figure 5.11 (c) and (d) show the topological phase for Weyl nodes with different chirality. For q outside the separatrix, change in topological phase is large and close to $\pm 2\pi$, while for the point q inside the separa-

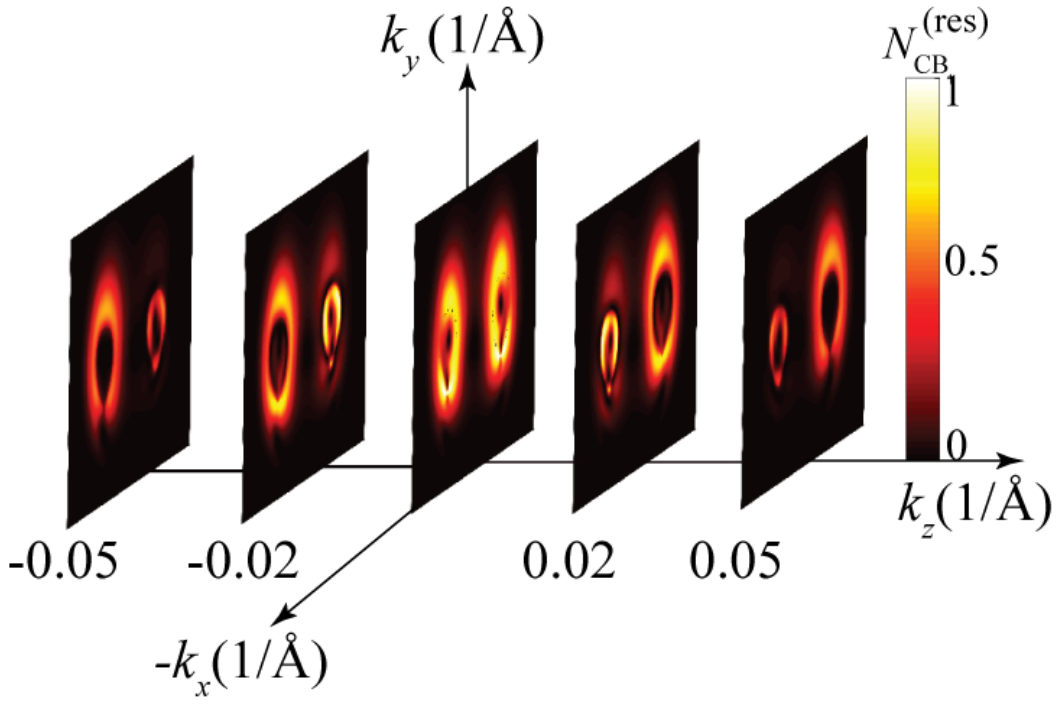

Figure 5.10 (Color online) Residual CB population as a function of (k_x, k_y) for different values of k_z in the reciprocal space after a single oscillation circularly polarized pulse. The pulse is incident normally on the system along the z direction. Field amplitude is $F_0 = 0.01$ V/Å.

trix change in topological phase is much smaller. The dynamic phase $\phi_{cv}^{(d)}(\mathbf{q}, t)$ (Eq. (5.15)) decreases with time t. Significant change ($\gtrsim 2\pi$) in total phase along the Bloch trajectory prevents accumulation of the conduction band population. In two cases, red line in Figure 5.11 (c) and black line in (d) topological phase increase and mutual cancellation of the dynamic phase and the topological phase enhances the conduction band population inside and outside of the separatrix at W and $W^{'}$, respectively. In contrast, the total phase for outside and inside the separatrix at W and $W^{'}$ points, change dramatically, and as a result, the conduction band population is almost zero at this region. In fact, the population is

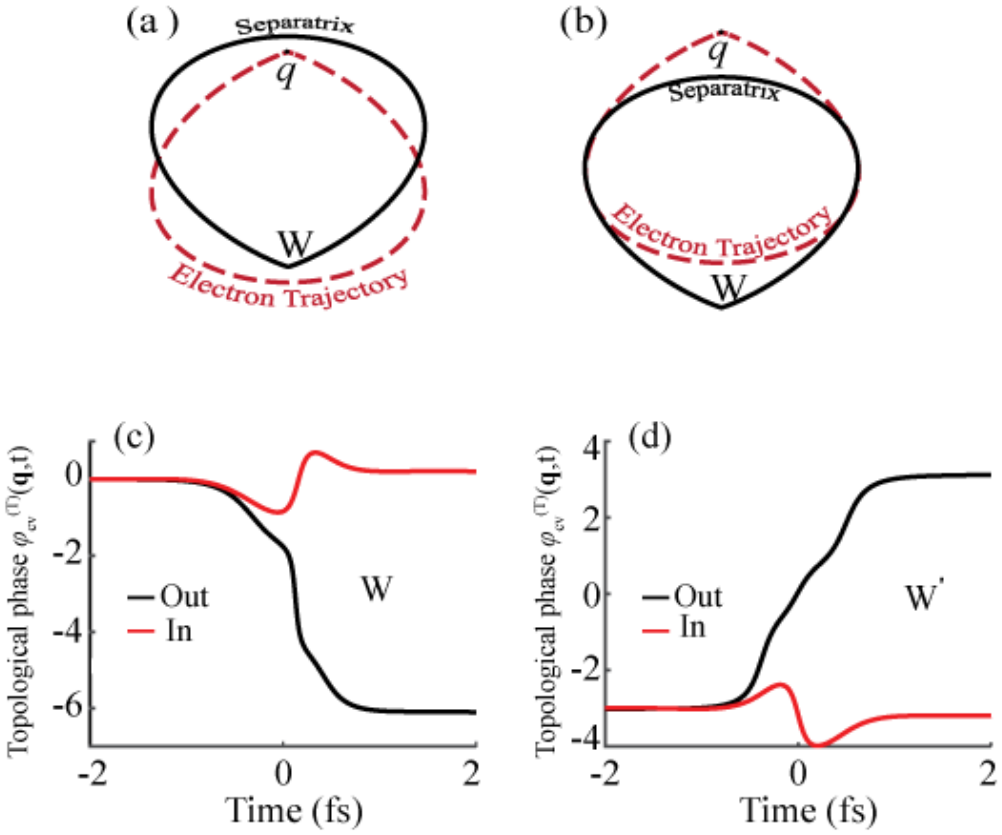

Figure 5.11 (Color online) Red dashed line shows the electron trajectory in reciprocal space which start and end at point q. In panel (a) q is inside the separatrix (black solid line) and its trajectory encircle the Weyl point ,W, but in panel (b) q is outside the separatrix and so its trajectory does not encircle the Weyl point.(c) Topological phase $\phi_{cv}^{(T)}(\mathbf{q}, t)$ on the Bloch trajectory for the W point for the initial point q outside of the separatrix (black line) and inside the separatrix (red line). (d) The same as (c) but for the W' point.

determined by the topological phase.

The topological resonances in the Weyl semimetals occur because of the finite effective bandgap, Δ, which is determined by the finite value of k_z, $\Delta \propto k_z$. By changing the sign of k_z, we change the sign of the effective bandgap and, correspondingly, the sign of the topological phase. As a results while for positive k_z the topological resonance is realized for

inside the separatrix for W point and outside of the separatrix for $W^{'}$ point, for negative k_z the topological resonance is realized outside and inside the separatrix for W and $W^{'}$ points, respectively. For left-handed circularly polarized (LCP) pulse the distribution of the electrons in the conduction band is mirror-symmetric with respect to the yz plane of that RCP pulse, which is due to the chirality selection rule [41].

5.3.2.2 Circularly polarized pulse with two oscillations

We assume a circularly polarized pulse consisting of two optical cycles is incident normally on the system along the z direction and has the following form

$$\begin{aligned} F_x(t) &= F_0[-e^{-u^2}(1-2u^2) \mp \alpha e^{-(u-u_0)^2}(1-2(u-u_0)^2)], \\ F_y(t) &= 2F_0[ue^{-u^2} + \alpha(u-u_0)e^{-(u-u_0)^2}], \end{aligned} \tag{5.30}$$

where $u = t/\tau$ and τ is set to 10 fs. We solve Eq. (5.19) with the initial condition $(\beta_{v\mathbf{q}}, \beta_{c\mathbf{q}}) = (1, 0)$. Figure 5.12 shows the momentum space interferogram near the Weyl points for a pulse consisting of two optical periods with different handedness. The amplitude of the second cycle is 75%, $\alpha = 0.75$, of the first cycle. The distribution is highly chiral and changing the circularity to the opposite would change the distribution of electron to be mirror-reflected in the yz plane, see Figure 5.12 (a) and (b). The interferogram at W and W' are different, reflecting the intrinsic chirality related to the Berry phase of Weyl semimetals in reciprocal space. This behavior is similar to graphene when a circularly polarized pulse consisting of

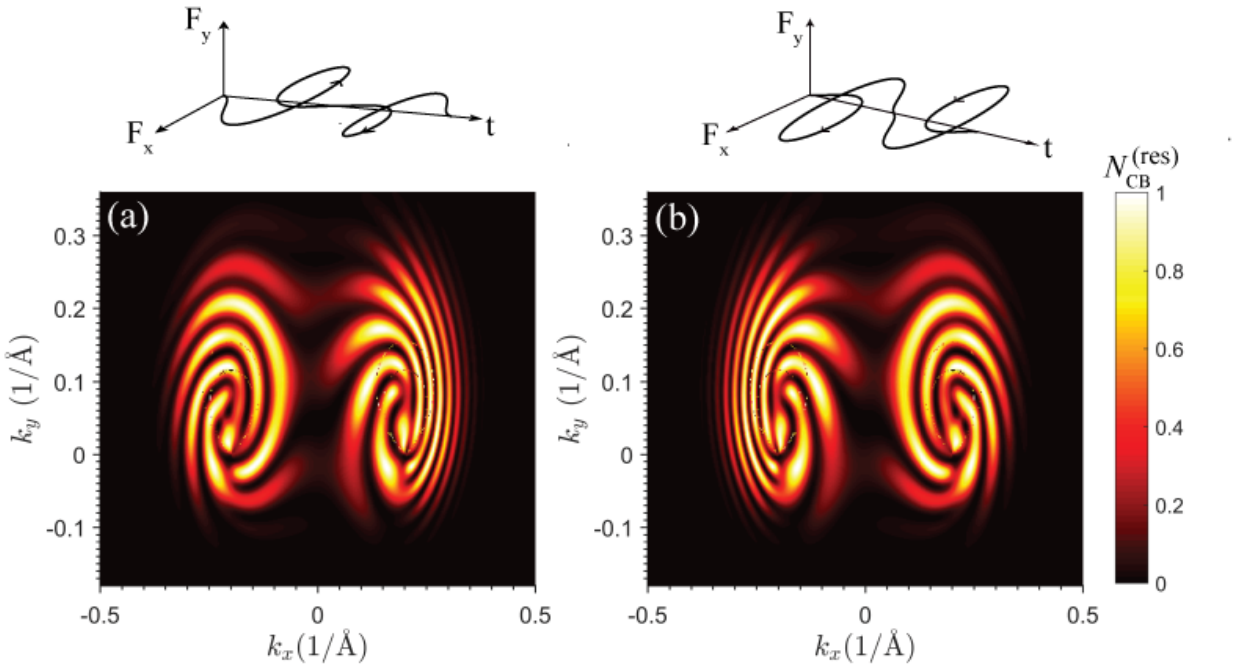

Figure 5.12 (Color online) Residual CB population as a function of **k** in reciprocal space for $k_z = 0$, after a two oscillations pulse.(a) The first optical cycle is right-handed circularly polarized with amplitude $F_0 = 0.01$ V/Å, and the second cycle is left-handed circularly polarized with amplitude $0.75F_0$. The position of two Weyl nodes in reciprocal space is $(\pm 0.2, 0, 0)$. (b) Same as (a) but for a pulse with opposite chirality. In the first oscillation, the electric field rotates clockwise while in the second oscillation it does so counter-clockwise.

two cycles with opposite circularities applied to the system[5]. At the end of the first cycle, $t = 30$ (fs), the pulse does populate the conduction band along the separatrix, see Figure. (5.9), but does not produce any interference fringes. The origin of the fringes is related to the passage of the second pulse. During the second optical pulse, whose circularity is opposite of the first optical pulse, gradually the formation of interference fringes starts in the direction of the electric field rotation along the second separatrix. The origin of chirality is related to

the different pathways that an electron moves during the two circular pulses. When the first optical pulse is applied, the electron starts at k_0 point in reciprocal space, then moves toward the Weyl point,W, where the transition between valence and conduction band occurs. At this point there are two possibilities: 1) the electron transfers to the conduction band with the corresponding amplitude A_1, 2) the electron stays in the valence band and completes the first cycle in the valence band with amplitude A_2 and transfer to the valence band during the second pulse. Then for both pathways at the end of the first pulse, the electron returns to the initial point, k_0, before continuing in the second cycle in the opposite direction of the first pulse. If time between the two passages of the W point is minimum, so any dephasing is small and causes the phase increases fastest along the separatrix. Some part of the fringes are normal to the separatrix which means phase increases fastest along the separatrix. For the k_0 points whose the time between the first and second passage of the W point increases up to the optical period, T, there is little phase-difference along the separatrices, and the fringes tend to be parallel to the separatrices. This interferometer does not need an external reference source and, therefore, is self-referenced. Figure 5.13 shows the fringes in reciprocal space for a pulse consisting of two subpulses with the same circularity and amplitude. In contrast to Figure (5.12), the optical pulse does not cause any interferogram chirality. This is due to the fact that in this case the time between the first and second passage of the electron through the W point is large and is exactly the period T, which cause strong dephasing and as a result the fringes is mostly parallel to the separatrix. Also, the field amplitudes for two oscillation are equal and so the probability amplitude of two different possibilities

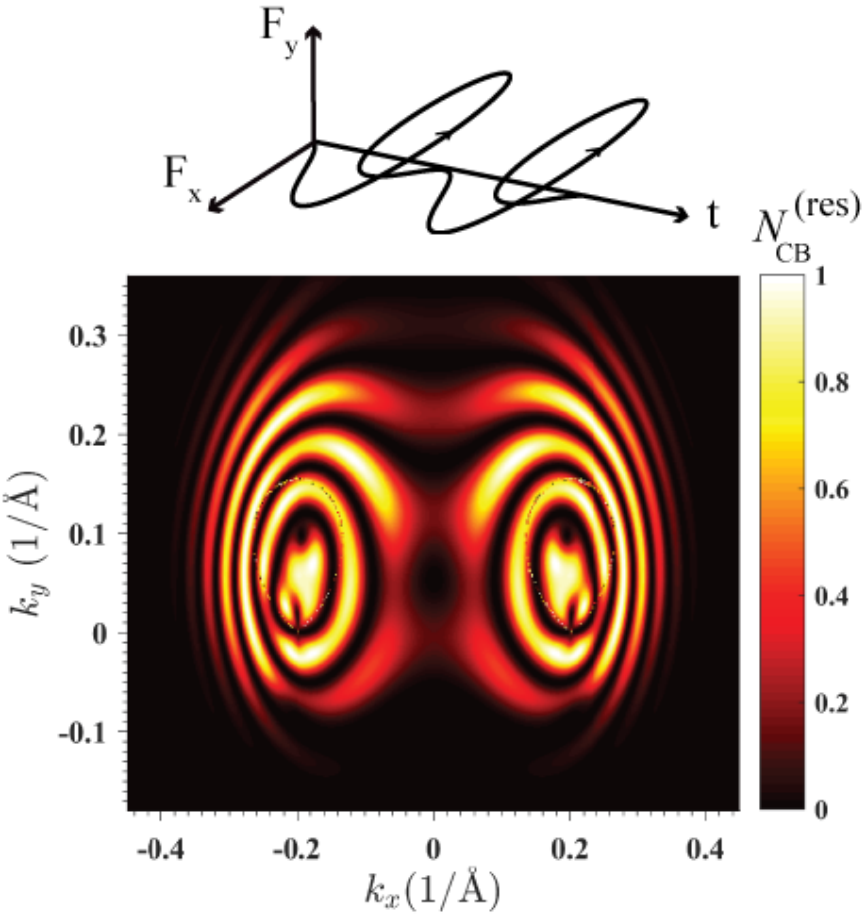

Figure 5.13 (Color online) Residual CB population as a function of **k** in reciprocal space for $k_z = 0$, after a two oscillations pulse.(a) Both optical cycles have the same chirality and amplitude, $\alpha = 1$. The field amplitude of the pulse is $F_0 = 0.01$ (V/Å).

explained above is related as $A_1 = A_2^*$, causes the distributions to be a chiral. However, the distributions for W and W' are still different which is due to the intrinsic chirality of Weyl points in reciprocal space.

5.3.2.3 Conclusion

In summary, we studied the electron dynamics of Weyl semimetals in a circularly polarized optical pulse with the duration of a few femtoseconds . One single oscillation circularly

polarized pulse causes the electrons to circle in the momentum space and accumulate both dynamic phase and topological Berry phase along the separatrix where the maximum transfer between the valence band and conduction band occur. We calculated the CB population for two cases: 1) $k_z = 0$ and 2) a non-zero value of k_z. For the first case, $k_z = 0$, the system is similar to graphene and the response of Weyl points to the ultrafast pulses are the same. In this case the topological phase is constant during the pulse and so both inside and outside of the separatrix is populated. However, with an increase k_z in the momentum space, the Weyl points behave differently to the external field. The significant property of the distribution of the electron in momentum space is that for a definite circular pulse, for one Weyl node the inside of the separatrix populates while for the other Weyl node the outside of the separatrix does populate. The distribution of CB population for non-zero value of k_z is the same as what we observed for gapped graphene [61]. For the case of gapped graphene by increasing gap, the response of Dirac points, K and K', to the ultrafast pulses with the definite circularity is different. While the pulse populates the inside of the separatrix in K point, the majority of the CB population is located outside of the separatriix for the K' point. Furthermore, employing a two-cycle circularly polarized pulse with opposite chirality and different amplitudes causes the formation of interferogram in reciprocal space which is highly chiral for two Weyl nodes and illustrates the intrinsic chirality of Weyl points in Weyl semimetals.

CHAPTER 6
CONCLUSIONS

In this dissertation, we study the interaction of phosphorene, a two-dimensional semiconductor matter with a band gap $\approx$ 2 eV, and Weyl semimetals, three-dimensional gapless matter, with an ultrafast laser field. Below I highlighted the most important results whcih we achieved in this dissertation:

• In chapter three we showed that the electron dynamics of a single layer of black phosphorous, phosphorene, in a strong field of an ultrashort optical pulse is highly irreversible. This irreversibility manifest itself as a finite residual conduction band population in the reciprocal space. Although the phosphorene has a relatively large bandgap, $\approx$ 2 eV, the irreversible electron dynamics in phosphorene is similar to the electron dynamics in other 2D materials, such as gapless graphene, silicene, or germanene.

• The distribution of the CB population in the reciprocal space shows hot spots that are located near the Γ point where the dipole coupling between the valence band and the conduction band is maximum. Also, during the pulse the electron passes the Γ point two times which causes the formation of hot spots.

• The external electric field induces the current through the system. The electric current has two contributions: interband and intraband. In our case of phosphrene, the main contribution to the electric current comes from the intraband.

In chapter four, first we study the interaction of Weyl semimetals in a strong linearly polarized ultrafast pulse. The results show that:

• The electron dynamics in such materials is coherent and highly anisotropic. For some directions of pulse polarization, the electric dynamics is irreversible. For other directions of polarization, the electron dynamic is highly reversible and, after the pulse, the electron system returns to its initial state with almost zero conduction band population. Such high anisotropy in electron dynamics is related to anisotropy in interband dipole matrix elements.

• In the reciprocal space, the electron conduction band population density shows hot spots near the Weyl points where the dipole coupling between the bands are large.

• The optical pulse also causes net charge transfer through the system. The direction of transfer is the same as the direction of the field maximum. The transferred charge has highly anisotropic dependence on polarization direction with almost zero transferred charge for some directions.

• In the next step we applied a circularly polarized pulse. The ultrafast pulse causes a finite electron conduction band population both during and after the pulse. We show that the electron dynamics is coherent and highly irreversible.

• For a pulse propagating in the z direction, the large population of electrons is located near the Weyl points and along the separatrix. For small k_z, the system behaves similar to graphene and, the interband dipole matrix elements are highly localized near the Weyl points.

• For nonzero k_z, the system is similar to graphene with a gap and the interband dipole matrix is delocalized. Therefore, the transformation of electrons between the valence band and the conduction band are not confined in a narrow region.

• The circularly femtosecond single oscillation pulse also induces charge transfer in both x and y directions through the system during the pulse. For both sets of Weyl points, charge transfer in both x and y directions increase with the field.

In chapter five we observed topological properties of Weyl semimetals by applying the linearly and circularly polarized pulse. The results is summarized as

• For $k_z = 0$, the response of Weyl points to an ultrafast pulse (both linearly and circularly polarized pulse) is similar and the distribution of the CB population near Weyl points are the same.

• With an increase k_z in the system, an ultrafast laser pulse with a duration of a few femtoseconds populates the area near the Weyl points differently which introduces topological resonances in the momentum space.

• The induction CB population in the reciprocal space is highly structured and is determined by the topological phase.

• The induction conduction band population by a circularly polarized pulse consisting of two oscillations with opposite chirality in the reciprocal space is highly chiral which represent the intrinsic chirality of the Weyl nodes.

REFERENCES

[1] A. Castellanos-Gomez, L. Vicarelli, E. Prada, J. O. Island, K. Narasimha-Acharya, S. I. Blanter, D. J. Groenendijk, M. Buscema, G. A. Steele, J. Alvarez, et al., Isolation and characterization of few-layer black phosphorus, 2D Materials 1 (2) (2014) 025001.

[2] E. T. Sisakht, M. H. Zare, F. Fazileh, Scaling laws of band gaps of phosphorene nanoribbons: A tight-binding calculation, Physical Review B 91 (8) (2015) 085409.

[3] F. Nematollahi, V. Apalkov, M. I. Stockman, Phosphorene in ultrafast laser field, Physical Review B 97 (3) (2018) 035407.

[4] H. K. Kelardeh, V. Apalkov, M. I. Stockman, Graphene in ultrafast and superstrong laser fields, Physical Review B 91 (4) (2015) 045439.

[5] H. K. Kelardeh, V. Apalkov, M. I. Stockman, Attosecond strong-field interferometry in graphene: Chirality, singularity, and berry phase, Physical Review B 93 (15) (2016) 155434.

[6] V. Apalkov, M. I. Stockman, Metal nanofilm in strong ultrafast optical fields, Physical Review B 88 (24) (2013) 245438.

[7] M. S. Wismer, S. Y. Kruchinin, M. Ciappina, M. I. Stockman, V. S. Yakovlev, Strong-field resonant dynamics in semiconductors, Physical review letters 116 (19) (2016) 197401.

[8] V. Apalkov, M. I. Stockman, Theory of dielectric nanofilms in strong ultrafast optical fields, Physical Review B 86 (16) (2012) 165118.

[9] S. Ghimire, G. Ndabashimiye, A. D. DiChiara, E. Sistrunk, M. I. Stockman, P. Agostini, L. F. DiMauro, D. A. Reis, Strong-field and attosecond physics in solids, Journal of Physics B: Atomic, Molecular and Optical Physics 47 (20) (2014) 204030.

[10] M. Breusing, S. Kuehn, T. Winzer, E. Malić, F. Milde, N. Severin, J. Rabe, C. Ropers, A. Knorr, T. Elsaesser, Ultrafast nonequilibrium carrier dynamics in a single graphene layer, Physical Review B 83 (15) (2011) 153410.

[11] A. Schiffrin, T. Paasch-Colberg, N. Karpowicz, V. Apalkov, D. Gerster, S. Mühlbrandt, M. Korbman, J. Reichert, M. Schultze, S. Holzner, et al., Optical-field-induced current in dielectrics, Nature 493 (7430) (2013) 70.

[12] M. Schultze, E. M. Bothschafter, A. Sommer, S. Holzner, W. Schweinberger, M. Fiess, M. Hofstetter, R. Kienberger, V. Apalkov, V. S. Yakovlev, et al., Controlling dielectrics with the electric field of light, Nature 493 (7430) (2013) 75.

[13] J. C. Johannsen, S. Ulstrup, F. Cilento, A. Crepaldi, M. Zacchigna, C. Cacho, I. E. Turcu, E. Springate, F. Fromm, C. Raidel, et al., Direct view of hot carrier dynamics in graphene, Physical Review Letters 111 (2) (2013) 027403.

[14] I. Gierz, J. C. Petersen, M. Mitrano, C. Cacho, I. E. Turcu, E. Springate, A. Stöhr, A. Köhler, U. Starke, A. Cavalleri, Snapshots of non-equilibrium dirac carrier distributions in graphene, Nature materials 12 (12) (2013) 1119.

[15] K. S. Novoselov, V. Fal, L. Colombo, P. Gellert, M. Schwab, K. Kim, et al., A roadmap for graphene, nature 490 (7419) (2012) 192.

[16] D. Jariwala, V. K. Sangwan, L. J. Lauhon, T. J. Marks, M. C. Hersam, Emerging device

applications for semiconducting two-dimensional transition metal dichalcogenides, ACS nano 8 (2) (2014) 1102–1120.

[17] K. Novoselov, A. Mishchenko, A. Carvalho, A. C. Neto, 2d materials and van der waals heterostructures, Science 353 (6298) (2016) aac9439.

[18] Q. H. Wang, K. Kalantar-Zadeh, A. Kis, J. N. Coleman, M. S. Strano, Electronics and optoelectronics of two-dimensional transition metal dichalcogenides, Nature nanotechnology 7 (11) (2012) 699.

[19] S. A. O. Motlagh, J.-S. Wu, V. Apalkov, M. I. Stockman, Femtosecond valley polarization and topological resonances in transition metal dichalcogenides, Physical Review B 98 (8) (2018) 081406.

[20] F. Bloch, Über die quantenmechanik der elektronen in kristallgittern, Zeitschrift für physik 52 (7-8) (1929) 555–600.

[21] W. Houston, Acceleration of electrons in a crystal lattice, Physical Review 57 (3) (1940) 184.

[22] K. S. Novoselov, A. K. Geim, S. V. Morozov, D. Jiang, Y. Zhang, S. V. Dubonos, I. V. Grigorieva, A. A. Firsov, Electric field effect in atomically thin carbon films, science 306 (5696) (2004) 666–669.

[23] Y. Zhang, Y.-W. Tan, H. L. Stormer, P. Kim, Experimental observation of the quantum hall effect and berry's phase in graphene, nature 438 (7065) (2005) 201.

[24] H. Ramakrishna Matte, A. Gomathi, A. K. Manna, D. J. Late, R. Datta, S. K. Pati, C. Rao, Mos2 and ws2 analogues of graphene, Angewandte Chemie International Edition

49 (24) (2010) 4059–4062.

[25] K. I. Bolotin, K. Sikes, Z. Jiang, M. Klima, G. Fudenberg, J. Hone, P. Kim, H. Stormer, Ultrahigh electron mobility in suspended graphene, Solid State Communications 146 (9-10) (2008) 351–355.

[26] M. Buscema, J. O. Island, D. J. Groenendijk, S. I. Blanter, G. A. Steele, H. S. van der Zant, A. Castellanos-Gomez, Photocurrent generation with two-dimensional van der waals semiconductors, Chemical Society Reviews 44 (11) (2015) 3691–3718.

[27] F. Koppens, T. Mueller, P. Avouris, A. Ferrari, M. Vitiello, M. Polini, Photodetectors based on graphene, other two-dimensional materials and hybrid systems, Nature nanotechnology 9 (10) (2014) 780.

[28] S. Z. Butler, S. M. Hollen, L. Cao, Y. Cui, J. A. Gupta, H. R. Gutiérrez, T. F. Heinz, S. S. Hong, J. Huang, A. F. Ismach, et al., Progress, challenges, and opportunities in two-dimensional materials beyond graphene, ACS nano 7 (4) (2013) 2898–2926.

[29] F. Xia, H. Wang, D. Xiao, M. Dubey, A. Ramasubramaniam, Two-dimensional material nanophotonics, Nature Photonics 8 (12) (2014) 899.

[30] K. F. Mak, C. Lee, J. Hone, J. Shan, T. F. Heinz, Atomically thin mos 2: a new direct-gap semiconductor, Physical review letters 105 (13) (2010) 136805.

[31] A. Splendiani, L. Sun, Y. Zhang, T. Li, J. Kim, C.-Y. Chim, G. Galli, F. Wang, Emerging photoluminescence in monolayer mos2, Nano letters 10 (4) (2010) 1271–1275.

[32] V. Tran, R. Soklaski, Y. Liang, L. Yang, Layer-controlled band gap and anisotropic excitons in few-layer black phosphorus, Physical Review B 89 (23) (2014) 235319.

[33] L. Li, Y. Yu, G. J. Ye, Q. Ge, X. Ou, H. Wu, D. Feng, X. H. Chen, Y. Zhang, Black phosphorus field-effect transistors, Nature nanotechnology 9 (5) (2014) 372.

[34] H. Liu, A. T. Neal, Z. Zhu, Z. Luo, X. Xu, D. Tománek, P. D. Ye, Phosphorene: an unexplored 2d semiconductor with a high hole mobility, ACS nano 8 (4) (2014) 4033–4041.

[35] L. Kou, C. Chen, S. C. Smith, Phosphorene: fabrication, properties, and applications, The journal of physical chemistry letters 6 (14) (2015) 2794–2805.

[36] A. N. Rudenko, M. I. Katsnelson, Quasiparticle band structure and tight-binding model for single-and bilayer black phosphorus, Physical Review B 89 (20) (2014) 201408.

[37] H. Weyl, H. weyl, z. phys. 56, 330 (1929)., Z. Phys. 56 (1929) 330.

[38] H. B. Nielsen, M. Ninomiya, Absence of neutrinos on a lattice:(i). proof by homotopy theory, Nuclear Physics B 185 (1) (1981) 20–40.

[39] H. B. Nielsen, M. Ninomiya, Absence of neutrinos on a lattice:(ii). intuitive topological proof, Nuclear Physics B 193 (1) (1981) 173–194.

[40] S. Bertrand, I. Garate, R. Côté, Light-induced valley polarization in interacting and nonlinear weyl semimetals, Physical Review B 96 (7) (2017) 075126.

[41] C.-K. Chan, N. H. Lindner, G. Refael, P. A. Lee, Photocurrents in weyl semimetals, Physical Review B 95 (4) (2017) 041104.

[42] C.-K. Chan, P. A. Lee, K. S. Burch, J. H. Han, Y. Ran, When chiral photons meet chiral fermions: photoinduced anomalous hall effects in weyl semimetals, Physical review letters 116 (2) (2016) 026805.

[43] X. Wan, A. M. Turner, A. Vishwanath, S. Y. Savrasov, Topological semimetal and fermi-arc surface states in the electronic structure of pyrochlore iridates, Physical Review B 83 (20) (2011) 205101.

[44] C. C. Lee., Y. Su., H. S. Ming., et.al, Fermi surface interconnectivity and topology in weyl fermion semimetals taas, tap, nbas, and nbp, Phys. Rev. B 92 235104.

[45] C. P. Weber, B. S. Berggren, M. G. Masten, T. C. Ogloza, S. Deckoff-Jones, J. Madéo, M. K. Man, K. M. Dani, L. Zhao, G. Chen, et al., Similar ultrafast dynamics of several dissimilar dirac and weyl semimetals, Journal of Applied Physics 122 (22) (2017) 223102.

[46] A. Burkov, M. Hook, L. Balents, Topological nodal semimetals, Physical Review B 84 (23) (2011) 235126.

[47] B. Lv, N. Xu, H. Weng, J. Ma, P. Richard, X. Huang, L. Zhao, G. Chen, C. Matt, F. Bisti, et al., Observation of weyl nodes in taas, Nature Physics 11 (9) (2015) 724.

[48] B. Yan, C. Felser, Topological materials: Weyl semimetals, Annual Review of Condensed Matter Physics 8 (2017) 337–354.

[49] B. Lv, H. Weng, B. Fu, X. Wang, H. Miao, J. Ma, P. Richard, X. Huang, L. Zhao, G. Chen, et al., Experimental discovery of weyl semimetal taas, Physical Review X 5 (3) (2015) 031013.

[50] M. V. Berry, Quantal phase factors accompanying adiabatic changes, Proc. R. Soc. Lond. A 392 (1802) (1984) 45–57.

[51] Y. Aharonov, D. Bohm, Significance of electromagnetic potentials in the quantum theory, Physical Review 115 (3) (1959) 485.

[52] I. Sodemann, L. Fu, Quantum nonlinear hall effect induced by berry curvature dipole in time-reversal invariant materials, Physical review letters 115 (21) (2015) 216806.

[53] T. Morimoto, S. Zhong, J. Orenstein, J. E. Moore, Semiclassical theory of nonlinear magneto-optical responses with applications to topological dirac/weyl semimetals, Physical Review B 94 (24) (2016) 245121.

[54] J. E. Moore, J. Orenstein, Confinement-induced berry phase and helicity-dependent photocurrents, Physical review letters 105 (2) (2010) 026805.

[55] L. Wu, S. Patankar, T. Morimoto, N. L. Nair, E. Thewalt, A. Little, J. G. Analytis, J. E. Moore, J. Orenstein, Giant anisotropic nonlinear optical response in transition metal monopnictide weyl semimetals, Nature Physics 13 (4) (2017) 350.

[56] K. Sun, S.-S. Sun, L.-L. Wei, C. Guo, H.-F. Tian, G.-F. Chen, H.-X. Yang, J.-Q. Li, Circular photogalvanic effect in the weyl semimetal taas, Chinese Physics Letters 34 (11) (2017) 117203.

[57] M. Z. Hasan, S.-Y. Xu, I. Belopolski, S.-M. Huang, Discovery of weyl fermion semimetals and topological fermi arc states, Annual Review of Condensed Matter Physics 8 (2017) 289–309.

[58] C.-C. Lee, S.-Y. Xu, S.-M. Huang, D. S. Sanchez, I. Belopolski, G. Chang, G. Bian, N. Alidoust, H. Zheng, M. Neupane, et al., Fermi surface interconnectivity and topology in weyl fermion semimetals taas, tap, nbas, and nbp, Physical Review B 92 (23) (2015) 235104.

[59] D. Xiao, M.-C. Chang, Q. Niu, Berry phase effects on electronic properties, Reviews of

modern physics 82 (3) (2010) 1959.

[60] A. Abrikosov, Methods of quantum field theory in statistical physics.

[61] S. Motlagh, V. Apalkov, M. I. Stockman, Ultrafast topological phenomena in gapped graphene, arXiv preprint arXiv:1812.08812.